Spray Coating Experiments: Setups and Methodologies

The latest eBook from Advanced Optical Metrology. Download for free.

Spray Coating Experiments: Setups and Methodologies, is the third in our Thin Films eBook series. This publication provides an introduction to spray coating, three article digests from Wiley Online Library and the latest news about Evident's Image of the Year Award 2022.

Wiley in collaboration with Evident, are committed to bridging the gap between fundamental research and industrial applications in the field of optical metrology. We strive to do this by collecting and organizing existing information, making it more accessible and useful for researchers and practitioners alike.

EVIDENT
OLYMPUS

WILEY

NANO · MICRO small
www.small-journal.com

Stimuli-Responsive Multifunctional Nanomedicine for Enhanced Glioblastoma Chemotherapy Augments Multistage Blood-to-Brain Trafficking and Tumor Targeting

Cláudia Martins, Marco Araújo, Alessio Malfanti, Catarina Pacheco, Stuart J. Smith, Bernard Ucakar, Ruman Rahman, Jonathan W. Aylott, Véronique Préat, and Bruno Sarmento**

Minimal therapeutic advances have been achieved over the past two decades for glioblastoma (GBM), which remains an unmet clinical need. Here, hypothesis-driven stimuli-responsive nanoparticles (NPs) for docetaxel (DTX) delivery to GBM are reported, with multifunctional features that circumvent insufficient blood-brain barrier (BBB) trafficking and lack of GBM targeting—two major hurdles for anti-GBM therapies. NPs are dual-surface tailored with a i) brain-targeted acid-responsive Angiopep-2 moiety that triggers NP structural rearrangement within BBB endosomal vesicles, and ii) L-Histidine moiety that provides NP preferential accumulation into GBM cells post-BBB crossing. In tumor invasive margin patient cells, the stimuli-responsive multifunctional NPs target GBM cells, enhance cell uptake by 12-fold, and induce three times higher cytotoxicity in 2D and 3D cell models. Moreover, the in vitro BBB permeability is increased by threefold. A biodistribution in vivo trial confirms a threefold enhancement of NP accumulation into the brain. Last, the in vivo antitumor efficacy is validated in GBM orthotopic models following intratumoral and intravenous administration. Median survival and number of long-term survivors are increased by 50%. Altogether, a preclinical proof of concept supports these stimuli-responsive multifunctional NPs as an effective anti-GBM multistage chemotherapeutic strategy, with ability to respond to multiple fronts of the GBM microenvironment.

1. Introduction

According to the Global Cancer Observatory 2020, the incidence of brain cancers is currently averaging 300 000 new cases per year, associated with 250 000 deaths worldwide.[1] From this, glioblastoma (GBM) is the most prevalent and lethal type of brain cancer, with less than 15 month median survival.[2] The current standard of care relies on surgical resection, followed by radiotherapy and temozolomide (TMZ) chemotherapy. TMZ presents an unique capacity to cross the blood-brain barrier (BBB), but also well-reported mechanisms of resistance and a poor tumoricidal potency highlighted by an IC_{50} of approximately 800×10^{-6} M (U-87 MG GBM cell line).[3] Therefore, avenues are open for exploiting more tumoricidal chemotherapeutics such as docetaxel (DTX), which presents an IC_{50} of only 0.04×10^{-6} M (U-87 MG GBM cell line).[3] However, key challenges to address reside on circumventing

C. Martins, M. Araújo, C. Pacheco, B. Sarmento
i3S - Instituto de Investigação e Inovação em Saúde
Universidade do Porto
Rua Alfredo Allen 208, Porto 4200-393, Portugal
E-mail: bruno.sarmento@ineb.up.pt

C. Martins, M. Araújo, C. Pacheco, B. Sarmento
INEB - Instituto Nacional de Engenharia Biomédica
Universidade do Porto
Rua Alfredo Allen 208, Porto 4200-393, Portugal

C. Martins
ICBAS – Instituto de Ciências Biomédicas Abel Salazar
Universidade do Porto
Rua de Jorge Viterbo Ferreira 228, Porto 4050-313, Portugal

The ORCID identification number(s) for the author(s) of this article can be found under https://doi.org/10.1002/smll.202300029.

DOI: 10.1002/smll.202300029

A. Malfanti, B. Ucakar, V. Préat
Advanced Drug Delivery and Biomaterials
Louvain Drug Research Institute
University of Louvain
Brussels 1200, Belgium
E-mail: veronique.preat@uclouvain.be

C. Pacheco, B. Sarmento
CESPU - Instituto de Investigação e Formação Avançada em Ciências e Tecnologias da Saúde
Rua Central de Gandra 1317, Gandra 4585-116, Portugal

S. J. Smith, R. Rahman
School of Medicine
University of Nottingham Biodiscovery Institute
Children's Brain Tumour Research Centre
University Park
Nottingham NG7 2RD, UK

J. W. Aylott
School of Pharmacy
Boots Science Building
University of Nottingham
Nottingham NG7 2RD, UK

the principal pharmaceutical constrains of DTX, which include a i) suboptimal aqueous solubility, ii) poor BBB permeation—blood plasma to cerebrospinal fluid ratio of 0.001–0.09 versus 0.2–0.3 for TMZ[4] -, and lack of GBM cell accumulation post-BBB crossing—1% tumor tissue uptake of the total dose.[5]

Over recent years, targeted cancer nanomedicine has provided multi-component nanoparticle (NP) systems with the ultimate goal of improving the biological performance of difficult-to-deliver cargos, such as DTX. NP nanomedicines are able to counterattack the principal pharmaceutical constraints of DTX by providing i) safekeeping depot systems that enhance drug solubilization, ii) shuttling vehicles across biological barriers that improve drug bioavailability at the site of interest, and iii) a navigation function for tissue targeting and/or accumulation enhancement purposes.[6] In the field of cancer nanomedicine, the biocompatible, biodegradable and Food and Drug Administration (FDA)-approved poly(lactic-co-glycolic acid) (PLGA) polymer has been widely explored as a matrix for NP assembly.[7] One of the gold standard modifications for PLGA NP systems relies on its combination with polyethylene glycol (PEG), which endows PLGA NPs with a plethora of surface tailoring options by functionalization of the PEG outer arms.[8]

Surface tailoring has been key to modulate the responsiveness of nanomedicines, such as PLGA/PEG NPs, to specific biologic stimuli. Ligand moieties are typically attached to the NP surface to recognize strategic cell transporters preferentially present or overexpressed at the target tissue, leading to higher drug accumulation at the target site, improved therapeutic responses, and reduced off-target effects. On the other hand, nanomedicines have been surface-tailored to take advantage of pH gradients naturally inherent to certain microenvironments, such as cell machinery compartments or tumors. Focusing on cell machinery compartments in light of the interest of this work, nanomedicines with acid-cleavable features have been proved promising to stimuli-triggered drug delivery since early and late endosomes are characterized by a pH 4.5–6.5.[9] An optimal NP design relies on systems with sufficient stability under near-neutral physiological conditions, and capable of a triggered response upon endosomal trafficking through the use of acid-cleavable chemical bonds. As an example, this could cause NP structural rearrangement in order to cleave and consequently remove a first surface layer, and expose a second surface layer, hence escaping the setback of steric hindrance. Acid-cleavable chemical bonds used for this purpose include acetals and hydrazones, typically hydrolyzed under pH 5 and 5.5 in approximately 6 min and 3 h, respectively.[10]

Herein, we propose a novel intravenous therapy for GBM based on a stimuli-responsive multifunctional PLGA/PEG NP platform encapsulating DTX and fostering the perfect symbiosis between BBB targeting and endocytosis, structural rearrangement within the acidic pH of BBB endosomes, and enhancement of GBM cell accumulation post-BBB trafficking. The proposed NPs will present a PLGA core alongside with i) an acid-cleavable long-length PEG shielding coupled with a first targeting ligand, Angiopep-2 peptide, to target the BBB-overexpressed low-density lipoprotein receptor (LDLR) and trigger blood-to-brain endocytosis,[11] and ii) a short-length PEG shielding coupled with a second targeting ligand, L-Histidine (termed His), to target the tumor-overexpressed L-type amino acid transporter 1 (LAT1)[12] and trigger BBB-to-GBM transport. Angiopep-2 has been one of the most exploited LDLR-ligands in the field of brain-targeted nanomedicine due to its proven capability of shuttling nanosystems across the BBB via LDLR and, consequently, increase the endocytosis and/or transcytosis rates by several-fold.[11] Whereas, LAT1 is a promising target for GBM therapies, extensively reported to be overexpressed by GBM cells[12]—analysis of clinical samples confirmed that LAT1 is significantly overexpressed in high-grade gliomas, expressed in lower levels in low-grade gliomas, and expressed only in basal levels in the normal cerebral cortex (Figure S1, Supporting Information). The NP acid-cleavable properties will assure that the long-length PEG-Angiopep-2 separates from the NP structure after encountering the acid pH of endosomes during BBB trafficking to facilitate endosomal escape and NP expulsion towards the brain.[13] On the other hand, the difference of PEG length will assure that, after separation of the long-length PEG shielding from the NP structure, the second targeting ligand, His, coupled with a PEG shielding of short length, is surface exposed due to steric de-protection. This is the first time that a multi-ligand functionalized NP system is proposed to sequentially target the BBB and GBM through the exploitation of a BBB-responsive transport mechanism. Over the last 10 years, other authors exploited multi-ligand functionalization of therapeutic NPs for BBB and GBM targeting,[14] but none of these systems presented BBB-stimulus responsiveness to boost NP permeation across the BBB,[13,15] paving the way to allow tumor-targeted loaded cargos to exert an enhanced anti-GBM effect. In this work, targeting polymeric conjugates with Angiopep-2 and His moieties were chemically synthesized to assemble the stimuli-responsive multifunctional NPs, which were further evaluated regarding cell uptake and cytotoxicity in 2D and 3D models of conventional cell lines and GBM invasive margin (GIN) patient cells, and BBB permeability. Moreover, in vivo biodistribution and therapeutic efficacy studies following intratumoral and intravenous administration were performed to provide a preclinical proof of concept. A schematic illustration is displayed in **Figure 1**A.

2. Results and Discussion

2.1. Chemical Synthesis of Nanoparticle Targeting Polymeric Conjugates

PLGA–PEG polymers were functionalized with His or Angiopep-2 to trigger tumor accumulation and BBB permeation, respectively. The molecular weight (MW) of PEG within each targeting polymeric conjugate was specifically chosen to provide two levels of NP surface decoration, thus avoiding intersteric hindrance—a lower MW 2K PEG embedded within a PLGA-PEG(2K) polymer was used for His attachment, whereas a higher MW 5K PEG embedded within a PLGA-PEG(5K) polymer was used for Angiopep-2 attachment. For the Angiopep-2 functionalization, two different conjugates were synthesized, presenting either acid-cleavable or noncleavable properties.

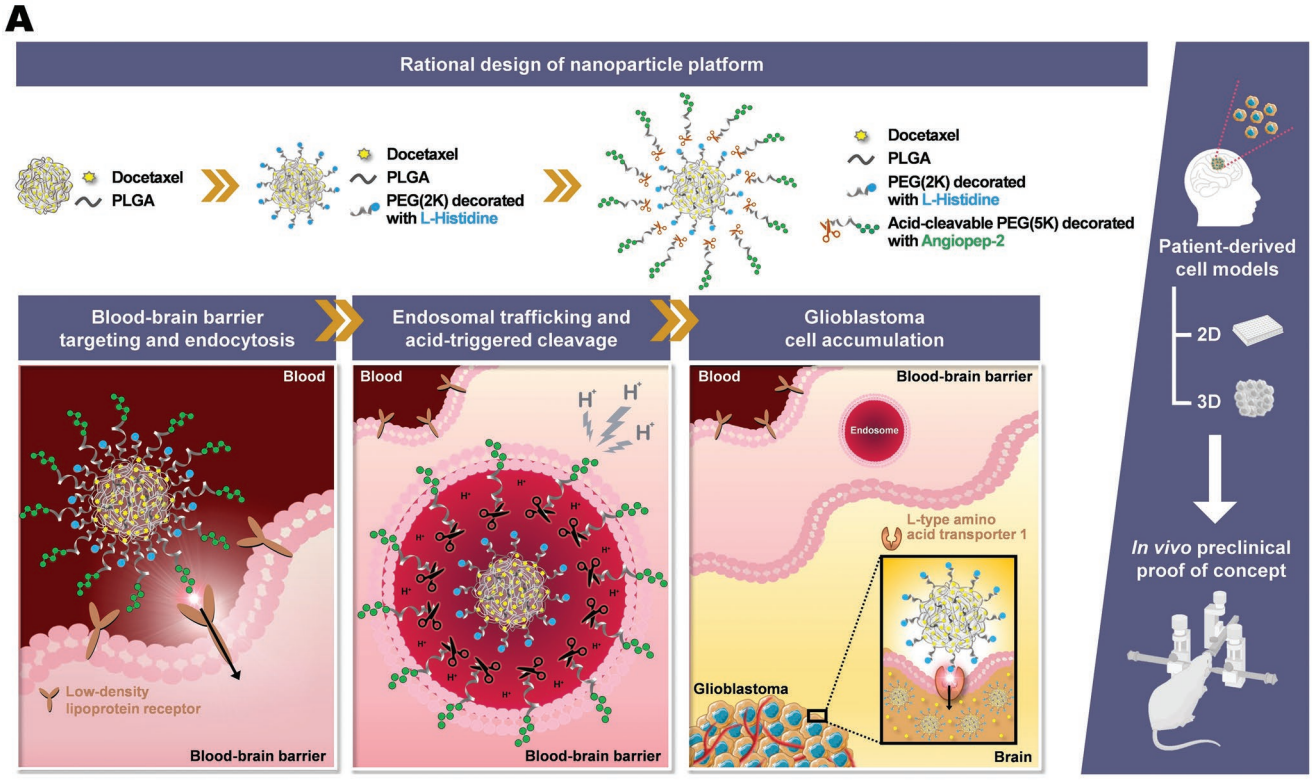

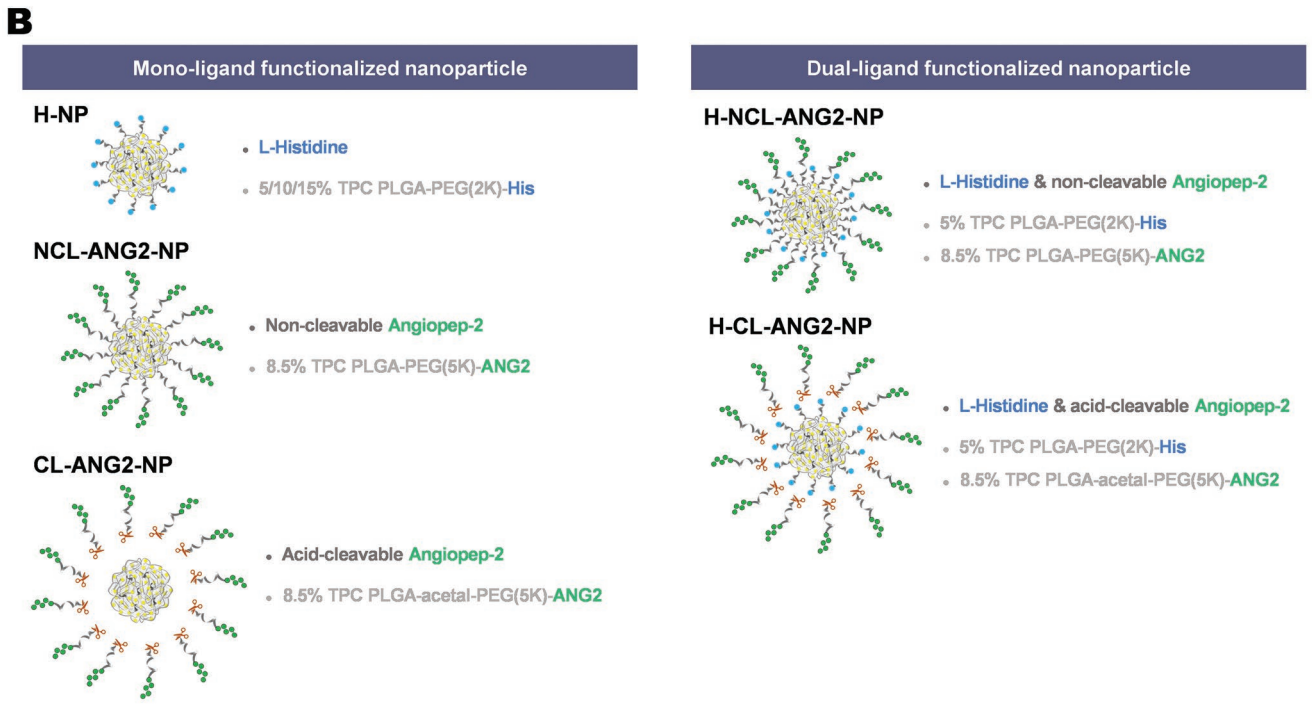

Figure 1. A) Schematic illustration of the proposed stimuli-responsive multifunctional NP platform design and hypothesized biological mechanism of action. B) Monoligand or dual-ligand surface functionalized NP formulations herein manufactured, and respective composition and designation.

2.1.1. L-Histidine Functionalized Targeting Polymeric Conjugate

First, a PLGA-PEG(2K)-NH_2 polymer was chemically functionalized with COOH-Histidine-BOC in the L isomeric form (COOH-His-BOC) by a carbodiimide strategy followed by a selective carbamate hydrolysis (**Figure 2**A). The presence of a −BOC group protecting the $-NH_2$ end-group of COOH-His-BOC assured a site-oriented functionalization, avoiding amino

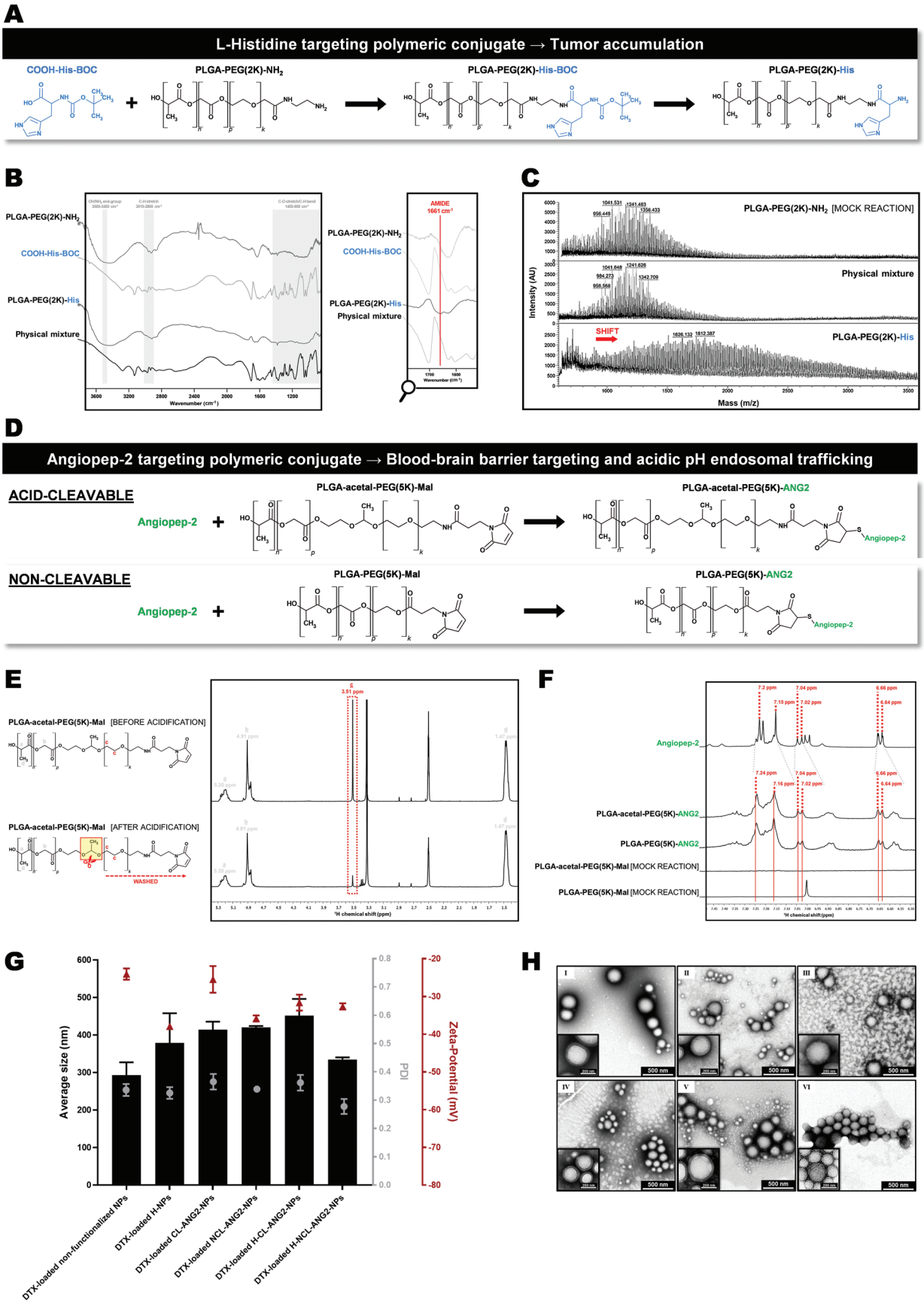

acid cross-reaction. PLGA-PEG(2K)-His-BOC FTIR demonstrated a similar fingerprint region to the PLGA-PEG(2K)-NH_2, comprising C—O stretching, C—N stretching, and C—H bending vibrations (Figure 2B).[16] Moreover, it was possible to observe a new band at 1661 cm^{-1} characteristic of C=O stretching in amides (amide I) in the spectrum of the PLGA-PEG(2K)-His-BOC, confirming the successful reaction between PLGA-PEG(2K)-NH_2 and COOH-His-BOC. PLGA-PEG(2K)-His-BOC ^{1}H NMR exhibited low-intensity characteristic peaks of COOH-His-BOC that were absent in the mock reaction control and shifted in comparison to COOH-His-BOC (δ = 7.58 versus 8.98 ppm; δ = 6.98 versus 8.34 ppm; δ = 6.80 versus 8.23 ppm; Figure S2, Supporting Information). The COOH-His-BOC ^{1}H NMR peaks at δ = 7.58 ppm and δ = 6.80 ppm are attributed to the imidazole ring protons of His, whereas the peak at δ = 6.98 ppm is attributed to the carbamate proton of the —BOC protecting group.[17] The ^{1}H NMR peak at δ = 1.35 ppm, characteristic of the —BOC methyl protons, was used to estimate the 90% COOH-His-BOC conjugation efficiency. In order to make the polymeric conjugate fully functional, the —BOC protecting group of PLGA-PEG(2K)-His-BOC was removed with success by a selective carbamate hydrolysis reaction, as revealed by ^{1}H NMR (Figure S3, Supporting Information). The MALDI-TOF MS spectrum of PLGA-PEG(2K)-His displayed an ionization profile clearly distinct not only from the PLGA-PEG(2K)-NH_2, but also from the physical mixture of PLGA-PEG(2K)-NH_2 and COOH-His-BOC (Figure 2C). Compared with PLGA-PEG(2K)-NH_2, it was observed a shift to higher *m/z* values, and a broader MW distribution, which corroborated a successful coupling of COOH-His-BOC with PLGA-PEG(2K)-NH_2. Water contact angle (WCA) confirmed an intermediate hydrophilicity degree for PLGA-PEG(2K)-His, compared with COOH-His-BOC and PLGA-PEG(2K)-NH_2 (Figure S4A,B, Supporting Information).

2.1.2. Angiopep-2 Functionalized Targeting Polymeric Conjugates—Cleavable versus Noncleavable

Second, thiol–Michael addition was selected to functionalize both PLGA-acetal-PEG(5K)-Mal and PLGA-PEG(5K)-Mal polymers with Angiopep-2 (giving PLGA-acetal-PEG(5K)-ANG2 and PLGA-PEG(5K)-ANG2, respectively), presenting acid-cleavable properties due the presence of the acid-cleavable acetal chemical group and non-cleavable properties, respectively. The Angiopep-2 was modified in advance with a N-terminal cysteine to assure a site-oriented functionalization, endowing the peptide with a —SH reaction site (Figure 2D). This modification is not expected to interfere with the Angiopep-2 biological activity since it was inspired by the strategy of Angiochem Inc. to develop an investigational chemotherapeutic drug under Phase III clinical trials, ANG1005, which consisted of Angiopep-2 modified with molecules of paclitaxel, namely at the N-terminus of the peptide.[18] 87% Angiopep-2 conjugation efficiency for PLGA-PEG(5K)-ANG2, and 86% for PLGA-acetal-PEG(5K)-ANG2, were estimated by Bradford assay in reaction supernatants. After media acidification (pH 5.5) and consecutive washings of the polymer, PLGA-acetal-PEG(5K)-ANG2 ^{1}H NMR revealed a significant decrease in the intensity of the PEG-related peak, which confirmed the acid-sensitive properties of the acetal group and consequent separation of the PEG(5K)-ANG2 moiety from the PLGA core polymer (Figure 2E). For both PLGA-acetal-PEG(5K)-ANG2 and PLGA-PEG(5K)-ANG2, ^{1}H NMR presented specific low-intensity Angiopep-2 characteristic peaks that were absent in the mock reaction controls (c.a. δ = 6.64, 6.66, 7.02, 7.04, 7.16, and 7.24 ppm), thus confirming the presence of the peptide in the structure of the polymeric conjugates (Figure 2F). Such peaks are characteristic of the aromatic ring protons from the phenylalanine and tyrosine amino acids of Angiopep-2.[19]

2.2. Nanoparticle Manufacture and Characterization

NP formulations were manufactured by a nanoprecipitation-on-chip using a continuous-flow microfluidic technique.[20] Lab-scale conventional methods to manufacture drug-loaded polymeric NPs lack full control over the process and are usually associated with low- and slow-throughput, limited loading of the cargo and batch-to-batch variability of NP critical quality attributes.[21] Thus, the continuous-flow technique herein applied takes advantage of a microfluidic chip that enables an automated and time-saving NP manufacturing process, while offering a reproducible in-house production of the nanomedicines, which is expected to facilitate future translation into clinics.[22] The total polymer content (TPC) of each formulation was tailored to manufacture distinct NP types, whose composition and designation are schematized in Figure 1B and summarized in **Table 1**.

All NP formulations presented, approximately, an average size range of 300 to 400 nm, 0.3 polydispersity index (PDI), and -35 to -25 mV zeta-potential (Figure 2G). Although the NP average size is not the standard for blood-to-brain crossing, considered to be around 50–100 nm,[23] a shift in paradigm has been observed in the field. Recently, BBB crossing has been reported as highly dependent on the equilibrium between NP size, stiffness, shape, and surface chemistry.[24] 500 nm NPs have been reported to transit across the BBB as efficiently as 100 nm NPs in terms of NP number, when undergoing receptor-mediated endocytosis and if presenting elastic moduli in the kPa–MPa range, as described for PLGA-PEG NPs.[24,25]

Figure 2. Polymeric conjugate chemical synthesis and NP assembly. PLGA-PEG(2K)-His A) chemical synthesis, B) FTIR characterization, and C) MALDI-TOF MS characterization. D) Scheme of the chemical synthesis of the Angiopep-2 functionalized targeting polymeric conjugates. E) ^{1}H NMR analysis of the acid-cleavable properties of the PLGA-acetal-PEG(5K)-Mal polymer used to further produce the PLGA-acetal-PEG(5K)-ANG2 targeting polymeric conjugate. F) ^{1}H NMR characterization of PLGA-acetal-PEG(5K)-ANG2 and PLGA-PEG(5K)-ANG2. G) Characterization of average size, PDI, and zeta-potential of the DTX-loaded NP formulations assembled from the chemically synthesized targeting polymeric conjugates. H) TEM characterization of the DTX-loaded NP formulations assembled from the chemically synthesized targeting polymeric conjugates, where I, II, III, IV, V, and VI correspond to non-functionalized NPs, H-NPs, CL-ANG2-NPs, NCL-ANG2-NPs, H-CL-ANG2-NPs, and H-NCL-ANG2-NPs, respectively.

Table 1. Polymeric conjugate percentage of TPC for each NP formulation, and respective designation. PEGylated NP controls were also manufactured using mPEG(2K)-PLGA or mPEG(5K)-PLGA, and termed mPEG(2K) NPs and mPEG(5K) NPs, respectively. NA: non-applicable.

	NP designation and polymeric conjugate composition (organic phase)				
	H-NP	CL-ANG2-NP	NCL-ANG2-NP	H-CL-ANG2-NP	H-NCL-ANG2-NP
PLGA-PEG(2K)-His	5%/ 10%/ 20%	NA	NA	5%	5%
PLGA-acetal-PEG(5K)-ANG2 (acid-cleavable)	NA	8.5%	NA	8.5%	NA
PLGA-PEG(5K)-ANG2 (non-cleavable)	NA	NA	8.5%	NA	8.5%

Depending on their surface chemistry, larger NPs might even deliver cargos more selectively to the targeted cells compared to their smaller counterparts.[26] Taken together, the average NP size range of 300 to 400 nm herein achieved was not considered an exclusion criterion per se, since the particles are expected to undergo LDLR-mediated endocytosis across the BBB via their Angiopep-2 moiety. The achieved size range, alongside with a PDI of around 0.3, are attributed to the high polymer concentration and consequent high viscosity of the organic phase used to manufacture the NPs.[27] This resulted from the attempt to provide a better entrapment phase to DTX and increase the loading degree, which usually does not exceed 1% for NPs with a PLGA-PEG matrix.[28]

Supporting Information presents detailed association efficiency and loading degree values for all formulations (Table S3, Supporting Information), as well as average size, PDI and zeta-potential complementary data (Figure S5, Supporting Information). Transmission electron microscopy (TEM) analysis revealed spherical shaped particles with relatively smooth surfaces, and a size distribution identical for all NP formulations (Figure 2H). The in vitro release profile of DTX was evaluated for 24 h under medium mimicking systemic physiological conditions. As depicted in Figure S6 (Supporting Information), NP formulations could retain part of DTX within their hydrophobic PLGA-based core, as about 60–80% of the drug was released in a sustained manner over the testing time window.

2.3. In Vitro Targetability in Glioblastoma Conventional Cell Lines and Invasive Margin Patient Cells—L-Histidine Functionalized Nanoparticles

A preliminary screening of the capacity of H-NPs to ameliorate the accumulation of the NPs into GBM cells was performed in GBM conventional cell lines, namely U-87 MG, U-251 MG, and U-373 MG. NPs were manufactured with different percentages of PLGA-PEG(2K)-His to understand the impact of the polymeric conjugate on cell-NP interaction. A protocol involving the use of trypsin for cell detachment prior to flow cytometry analysis was developed on purpose to remove the majority of membrane-bound NPs and enrich the signal in cell-internalized NPs.[29] Moreover, a preliminary cytotoxicity experiment was performed to find a non-cytotoxic NP dose (Figure S7, Supporting Information). As shown in **Figure 3**A, after 4 h treatment, H-NPs presented a significantly higher cell internalization compared to non-functionalized NPs, for all GBM cell lines. This was reflected by an increase of up to three times in both mean fluorescence intensity (MFI) and percentage of positive cells (Figure 3A and Figure S8, Supporting Information, respectively). We hypothesize that the increase in cell internalization is due to the capacity of the His moiety of NPs to recognize and bind LAT1, vastly reported to be overexpressed in human brain gliomas such as GBM, and directly associated with their excessive proliferation and malignant progression.[12] Previous RT-PCR studies reported that the LAT1 mRNA expression in the above-mentioned cell lines follows the order U-373 MG > U-251 MG > U-87 MG, which is in agreement with the trend of percentage of positive cells herein observed for H-NP cell internalization (U-373 MG > U-251 MG > U-87 MG, Figure S8, Supporting Information).[30] The L-isomeric form of His is extensively reported as one of the LAT1 substrates with highest affinity and stereoselectivity, presenting a kinetics K_m parameter of only 12.7×10^{-6} M, which is significantly lower compared to the K_m of other L-amino acid counterparts (e.g., 28.3×10^{-6} , 47.2×10^{-6} and 14.2×10^{-6} M for L-tyrosine, L-valine and L-phenylalanine, respectively).[31] Nevertheless, His or His-mimicking imidazole derivatives have been mostly exploited for their endosomal escape properties and pH-triggered conformational changes,[32] and not for the purpose of drug/NP accumulation into tumor cells such as of GBM. To our best knowledge, only one literature study associated the higher NP internalization of dendrimers modified with His with the general overexpression of amino acid transporters in HeLa cervical cancer cells, necessary for the rapid proliferation and increased antioxidant demands of these cells.[33] Other authors exploited LAT1-specific cancer cell delivery through the use of substrates with lower affinity for the transporter, such as glutamate[34] and L-tyrosine.[35] LAT1-specific delivery has also been widely explored in the field of positron emission tomography (PET) imaging for the detection of tumor tissues. PET probes modified with L-phenylalanine,[36] L-methionine,[37] and L-tyrosine[38] demonstrated precise tumor-specificity via binding of the amino acid constituents to LAT1.

However, the GBM tumor niche is characterized by a high level of heterogeneity and most of the conventional GBM cell lines are thought to have undergone genetic drift over the years, thus partially losing the invasive behavior characteristic

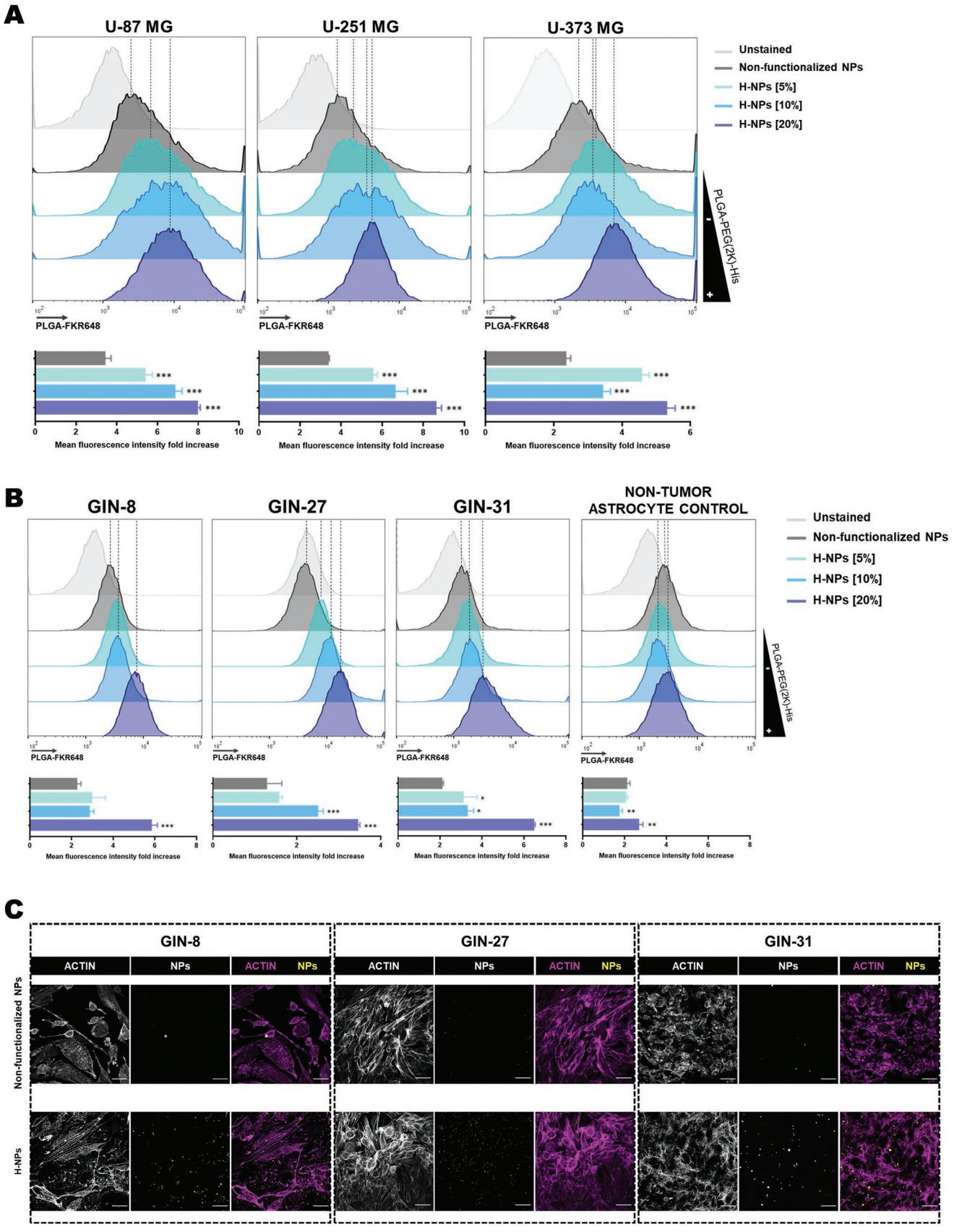

of GBM.[39] Moreover, these cell lines are derived from the core of the tumor, which does not realistically reflect the infiltrative behavior of post-surgical residual GBM cells.[40] Taken together, our efforts focused on using a complementary cell model for drug/NP testing, which could represent better the highly invasive and tumorigenic potential of GBM, such as GIN patient cells (Figure S9, Supporting Information).[41] GIN cells are isolated from the invasive margin of GBM tumor tissue of adult patients and evidenced by the 5ALA-Gliolan fluorescent region at surgery beyond the magnetic resonance imaging (MRI) T1 enhancing region.[41b] This invasive margin constitutes therapeutic resistant pressures, and is a molecular snapshot of recurrent tumor cells.[41] Three cell types were selected from the available GIN panel, namely GIN-8, GIN-27 and GIN-31. Similarly to what was observed for the GBM conventional cell lines, as shown in Figure 3B, after 4 h treatment, H-NPs presented a significantly higher cell uptake compared to non-functionalized NPs, for all GIN cell types. This was reflected by an increase of up to 3- and 12-fold in MFI and percentage of positive cells, respectively (Figure 3B and Figure S11, Supporting Information). Besides numerous studies on LAT1 overexpression in U-87 MG, U-251 MG and U-373 MG cells, also the GBM invasive margins have been widely described as areas of LAT1 overexpression.[42] In fact, the specific expression of LAT1 in human clinical samples was reported to be even higher in infiltrating glioma cells of the GBM invasive margin compared to glioma cells located at the tumor core.[42a] This explains the higher levels of cell internalization herein observed for H-NPs in GIN cells versus GBM conventional cell lines (U-87 MG, U-251 MG, U-373 MG), highlighted by the increase of up to 3- versus 12-times in the percentage of positive cells, respectively, compared to the non-functionalized NP control (Figures S8 and S11, Supporting Information). H-NPs composed by 20% PLGA-PEG(2K)-His were pre-selected for further studies based on the highest levels of cell uptake found in previous flow cytometry studies. H-NP cell uptake was then confirmed by confocal microscopy, where H-NPs presented a considerably higher cell overlapping compared with the nonfunctionalized NP control in all GIN cell types (Figure 3C and Figure S10, Supporting Information).

Last, as a proof of concept of cancer cell specificity, the cell internalization of H-NPs was assessed by flow cytometry in a non-tumor astrocyte control cell line. No biologically relevant differences were found between the cell internalization of H-NPs and non-functionalized NPs, as shown by the MFI values (Figure 3B). In what concerns the percentage of positive cells, H-NPs composed by 20% PLGA-PEG(2K)-His presented an increase of less than two times compared to the non-functionalized control, but only to a maximum of around 15% positive cells, which was attributed to non-specific binding (Figure S11, Supporting Information).

2.4. 2D/3D In Vitro Cytotoxicity and Invasion Potential in Glioblastoma Invasive Margin Patient Cells—L-Histidine Functionalized Nanoparticles

The in vitro pharmacological activity of the developed NP formulations was assessed in regard to their capacity to compromise the metabolic activity of GIN cells. Due to the highly invasive profile and key role in tumor recurrence,[43] GIN cells are expected to mimic better the treatment resistance faced by therapeutics in vivo.

GIN-8, GIN-27, and GIN-31 metabolic activity were evaluated after uninterrupted periods of treatment of 48 h and 96 h with DTX doses ranging from 0.45×10^{-9} M to 4.5×10^{-6} M. For all GIN cell types, the metabolic activity decreased in a dose-dependent manner, and lower levels were reached at 96 h (day 6) compared to 48 h (day 4). DTX-loaded H-NPs caused a similar impact on metabolic activity compared to DTX-loaded non-functionalized NPs and DTX-loaded mPEG(2K) NPs (**Figure 4**B, left panel). Moreover, DTX-loaded H-NPs demonstrated a similar or slightly lower decrease on cell metabolic activity compared to the non-nanoparticulate drug control, free DTX. This was expected since the assay conditions are static, thus, free drug molecules are readily available to interact with 2D cell monolayers in order to exert an anti-proliferative effect. Whereas, for the nanoparticulate samples, including DTX-loaded H-NPs, drug molecules become only available upon DTX diffusion across the porous PLGA matrix and, in a later stage, PLGA matrix erosion.[7]

After confirming the ability of DTX-loaded H-NPs to significantly decrease GIN cell metabolic activity, we hypothesized that 4 h dynamic-like boost treatments could give us more information about the adjuvant effect of the targeting strategy.[44] For the lowest concentration, 4.5×10^{-6} M DTX, none of the formulations was able to decrease the metabolic activity to values lower than 70% for all GIN cell types, including free DTX (Figure 4B, right panel). Thus, a higher concentration was tested, 45×10^{-6} M DTX, for which a significantly lower metabolic activity was observed for all GIN cell types treated with DTX-loaded H-NPs, in opposition to free DTX and the other NP controls, namely non-functionalized and PEGylated but non-targeted mPEG(2K) NPs (Figure 4B, right panel). This was attributed to the enhanced capacity of H-NPs of being internalized by GIN cells during a contact period of only 4 h, as demonstrated by previous flow cytometry studies, compared to non-functionalized NPs. Therefore, this led to a closer drug–cell interaction and, consequently, a more pronounced effect on the decrease of cell metabolic activity. The 45×10^{-6} M DTX boost treatment also implies a boost in the total number of NPs per area, which is hypothesized to benefit NP tumor cell uptake[45] compared to free DTX molecules, which did not present any biologically relevant advantage with respect to cell metabolic activity interference compared to the nanoparticulate samples.

Figure 3. Flow cytometry analysis of cell internalization of nonfunctionalized NPs and H-NPs assembled from 5%, 10% or 20% PLGA-PEG(2K)-His into A) GBM conventional cell lines (U-87 MG, U-251 MG, U-373 MG), and B) GIN patient cells (GIN-8, GIN-27, GIN-31) and non-tumor astrocytes. MFI values were normalized to the unstained control. Statistical comparison of H-NP groups with non-functionalized NPs. *$p < 0.05$, **$p < 0.01$, or ***$p < 0.001$. C) Confocal microscopy analysis of cell internalization of non-functionalized NPs and H-NPs assembled from 20% PLGA-PEG(2K)-His into GIN patient cells. Cell actin was stained to delineate the cell area and evidence its overlapping with PLGA-FKR648 labeled NPs. Scale bars represent 62 µm.

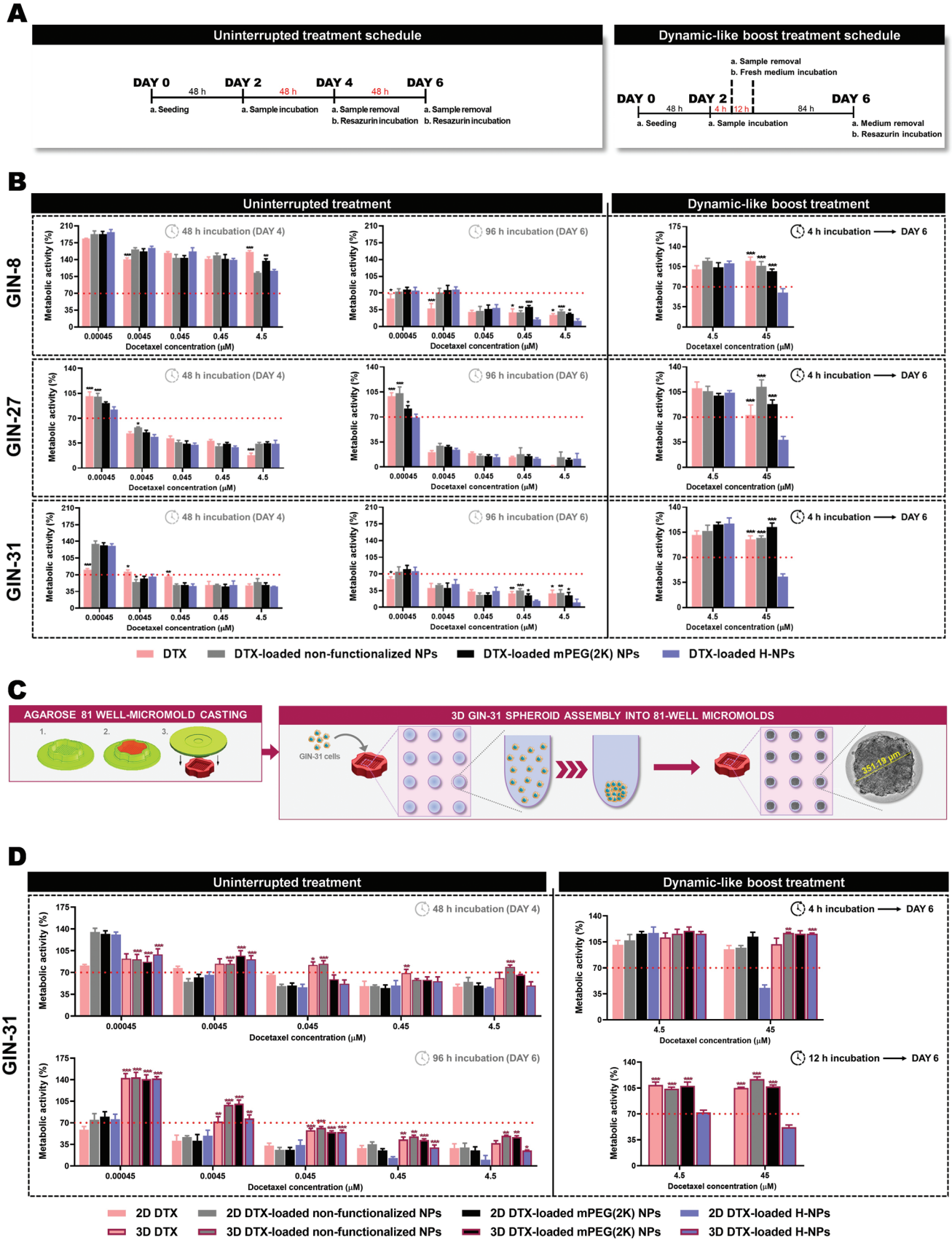

On the other hand, drug diffusivity and therapeutic effect within 3D cell cultures are more predictive of the potential in vivo response than simple 2D cultures. 2D cell cultures are considerably more sensitive to anticancer medicines compared to 3D counterparts, which behave similarly to human tumors presenting solid and bulky features, such as GBM.[39,46] Hence, we re-evaluated the previous 2D metabolic activity studies by selecting one of the GIN cell types, namely GIN-31, to assemble a 3D culture. GIN-31 tumor spheroids were generated by high-throughput microwell array technology using non-adhesive agarose hydrogels that promote cell aggregation into 3D spheroid structures with excellent size and shape reproducibility (Figure 4C).[47] After 48 h and 96 uninterrupted periods of treatment, GIN-31 spheroids followed the same trend observed for GIN-31 2D cultures, with the metabolic activity decreasing in a dose-dependent manner and lower levels reached at 96 h (day 6, Figure 4D, left panel). In general, the 3D metabolic activity values were higher compared to the 2D cell monolayer setting, which is potentially associated with the higher therapeutic resistance extensively reported for 3D cultures.[46,48] Similarly to 2D cultures, these uninterrupted periods of treatment did not evidence any biologically relevant differences between free DTX and the NP samples, although all of them resulted in a decrease of metabolic activity up to levels of approximately 35%. Next, we proceeded with the 4 h dynamic-like boost treatment and, herein, in opposition to 2D cultures, not even DTX-loaded H-NPs were able to lower cell metabolic activity (Figure 4D, right panel). This 2D versus 3D discrepancy is attributed to the insufficient drug penetration into the core of the GIN-31 spheroids over time due to their high interstitial pressure, reduced convective flow, and the presence of dense regions of extracellular matrix (ECM).[49] Thus, we challenged the spheroids with a broader time window of drug exposure, namely 12 h. In this case, it was possible to recover the significantly higher impact of DTX-loaded H-NPs on the decrease of cell metabolic activity of up to two times, as observed for 2D cultures, and became again clear the inability of free DTX or the other NP samples to provide the same effect (Figure 4D, right panel). H-NPs improved DTX transport across the spheroid structures most likely by promoting cell internalization via LAT1 binding, and an increased time exposure allowed DTX to reach deep regions of the spheroid tissue and recover the anti-proliferative effect on GIN-31 cells.

Additional data of the impact of the unloaded formulations on 2D and 3D cell metabolic activity can be found in Figures S12 and S13 (Supporting Information), respectively.

The impact of DTX-loaded H-NPs on the invasion ability of GIN-31 cells was further investigated in a Matrigel-coated Transwell assay (Figure S14, Supporting Information). DTX-loaded H-NPs provided three to four times lower percentage of invaded cells compared with the free DTX control and DTX-loaded non-functionalized NPs. Thus, the tumor targetability of H-NPs, which was shown to boost the inhibition of the metabolic activity of GIN-31 cells by DTX (Figure 4B), also enhanced the inhibition of GIN-31 cell invasion through an ECM-like in vitro matrix.

2.5. In vivo Therapeutic Efficacy after Intratumoral Administration—L-Histidine Functionalized Nanoparticles

The in vivo antitumor local effect of DTX-loaded H-NPs was validated in a GBM orthotopic mice model following an intratumoral treatment of 2 μg DTX per brain (**Figure 5**). After MRI assessment of tumor volume (Figure 5B) and group randomization at day 8, the formulations were administered intratumorally at day 10, and survival curves determined. Body weight was kept constant throughout 15 d postadministration, for all groups (Figure 5C). As presented in Figure 5D and **Table 2**, the median survival time was considerably improved by DTX-loaded H-NPs (46.5 d) compared to the untreated (30 d, $^{**}p < 0.01$), DTX-loaded non-functionalized NPs (33.5 d, $^{**}p < 0.01$), and free DTX (38 d) groups. Moreover, the DTX-loaded H-NP treatment resulted in a higher number of long-term survivors at 60 d (37.5% vs 0% for nonfunctionalized NPs) and 120 d (12.5% vs 0% for both nonfunctionalized NPs and free DTX). Thus, the DTX-loaded H-NP treatment significantly outperformed the DTX-loaded non-functionalized NP counterpart, which is consistent with in vitro studies. This was attributed to the ability of the His moiety to enhance GBM cell uptake, hence resulting in higher DTX accumulation at the tumor site and, consequently, a more potent therapeutic effect. It is of important note that overestimation of the therapeutic effect of free DTX is envisaged since the Taxotere vehicle used for DTX solubilization contains ethanol, which is used per se in the treatment of certain types of cancer via percutaneous injection (e.g., liver cancer, liver metastasis).[50] Overall, these findings offered robust evidence that, once inside the brain parenchyma, H-NPs are able to boost the chemotherapeutic effect of DTX and provide an in vivo therapeutic benefit.

2.6. In Vitro Permeability across the Blood-Brain Barrier—L-Histidine Plus Acid-Cleavable Angiopep-2 Functionalized Nanoparticles

A preliminary screening of BBB permeability was conducted in a standard hCMEC/D3 in vitro model to understand the ability

Figure 4. Evaluation of GIN cell metabolic activity after treatment with free DTX, DTX-loaded non-functionalized NPs, DTX-loaded mPEG(2K) NPs, and H-NPs composed by 20% PLGA-PEG(2K)-His. A) Treatment schedule. B) 2D metabolic activity of GIN patient cells (GIN-8, GIN-27, GIN-31). The left panel presents metabolic activity levels after uninterrupted periods of treatment of 48 and 96 h. The right panel presents a dynamic-like boost treatment of 4 h, integrated in an assessment period of incubation of 96 h. C) Assembly of GIN-31 tumor spheroids into high-throughput 81-well agarose micromolds–(1) molds (2) are filled with agarose, and (3) hydrogel micromolds obtained. The size of spheroids at the day of metabolic activity experiments averaged 350 μm. D) 3D metabolic activity of GIN-31 tumor spheroids. The left panel presents 2D versus 3D metabolic activity after uninterrupted periods of treatment of 48 and 96 h. The right panel presents a 2D versus 3D dynamic-like boost treatment of 4 h or 12 h, integrated in an assessment period of incubation of 96 h. Statistical comparison of DTX-loaded H-NPs with the other drug-loaded groups, within each dose range. $^{*}p < 0.05$, $^{**}p < 0.01$, or $^{***}p < 0.001$.

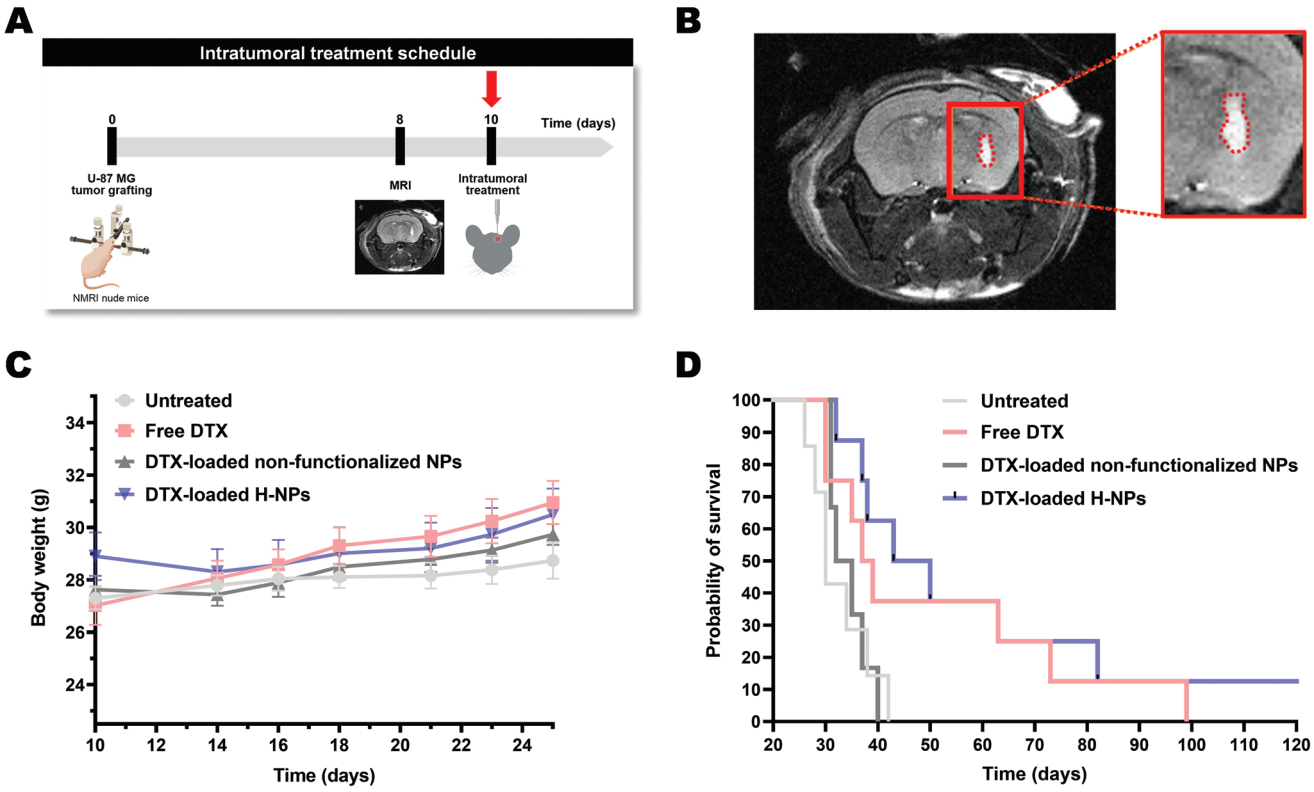

Figure 5. In vivo therapeutic efficacy of H-NPs after intratumoral administration. NMRI nude mice were orthotopically grafted with U-87 MG GBM cells at day 0, randomized upon MRI tumor evaluation at day 8, and treated with a dose of 2 µg DTX per brain at day 10. A) Treatment schedule. B) Representative mouse brain MRI of the U-87 MG GBM orthotopic model. C) Body weight follow-up until day 25. D) Mice survival curves until day 120.

of Angiopep-2 to ameliorate the accumulation of the NPs into the brain, the additional effect of His, as well as possible differences between acid-cleavable versus noncleavable Angiopep-2 moieties. The optimal Angiopep-2 density for BBB permeability reported in literature data in regard to the TPC of the formulation is highly variable, ranging from around 3% to 20%.[51] Thus, we set it up as 8.5% with the ultimate goal of assessing whether this percentage would be already sufficient to potentiate BBB permeability, before testing other percentages.

As displayed in **Figure 6**A, and surprisingly, the permeability of NCL-ANG2-NPs presented minimum advantage over non-functionalized NPs and PEGylated but non-targeted mPEG(5K) NPs. This can relate to the findings of Tian and co-workers, who demonstrated that Angiopep-2 density on NP surface should be carefully designed in order to avoid ligand-LDLR high avidity and consequent BBB endothelial cell internalization leading to fast degradation but, instead, favor mid avidity to increase the formation of syndapin-2 tubular structures leading to fast shuttling

Table 2. Resume of median survival, and percentage of survivors at 60 and 120 d (long-term survivors) for the in vivo therapeutic efficacy studies (intratumoral and intravenous treatment). Intratumoral treatment: statistical comparison of DTX-loaded H-NPs with untreated and DTX-loaded non-functionalized NPs groups (**$p < 0.01$). Intravenous treatment: statistical comparison of DTX-loaded H-CL-ANG2-NPs with the untreated group (*$p < 0.05$). NA: nonapplicable.

Treatment type	Treatment group	Median survival [days]	Percentage of survivors at 60 d [%]	Percentage of survivors at 120 d [%]
Intratumoral	Untreated	30	0	0
	Free DTX	38	37.5	0
	DTX-loaded non-functionalized NPs	33.5	0	0
	DTX-loaded H-NPs	46.5**	37.5	12.5
Intravenous	Untreated	37	0	NA
	Free DTX	43	20	NA
	DTX-loaded non-functionalized NPs	38	0	NA
	DTX-loaded H-NPs	40.5	20	NA
	DTX-loaded H-NCL-ANG2-NPs	41	20	NA
	DTX-loaded H-CL-ANG2-NPs	54*	50	NA

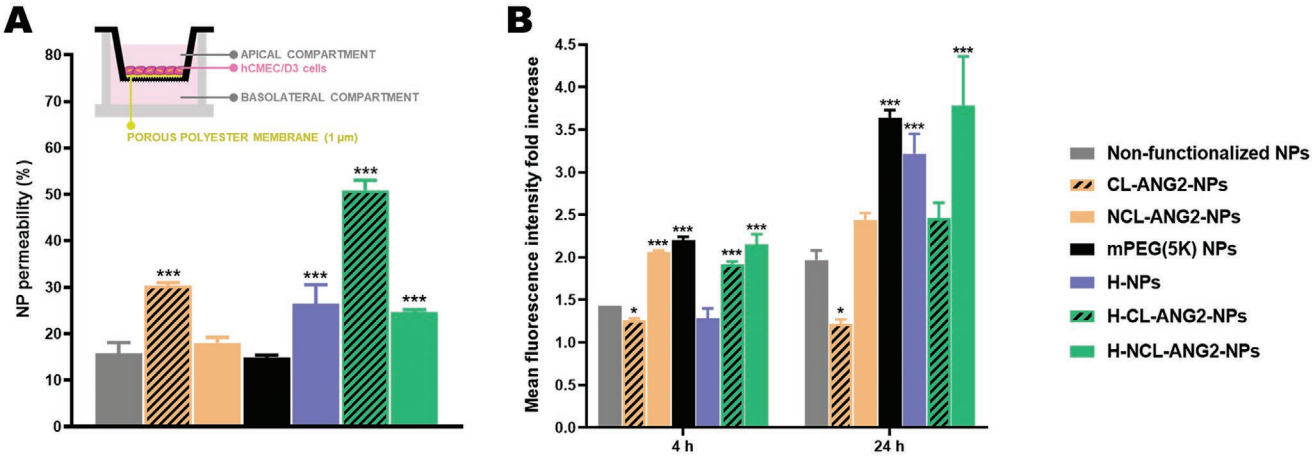

Figure 6. A) Evaluation of NP permeability across a BBB in vitro model, indicating the percentage of NP basolateral permeability across a hCMEC/D3 endothelial cell monolayer, normalized to the initial mass of NPs in the apical compartment. B) Flow cytometry analysis of cell internalization levels of NP formulations into BBB hCMEC/D3 endothelial cells. Statistical comparison of each group with non-functionalized NPs. *$p < 0.05$, **$p < 0.01$, or ***$p < 0.001$.

across the BBB.[13] Moreover, H-NPs presented a slightly 1.6-times higher BBB permeability compared to NCL-ANG2-NPs (Figure 6A), which can be explained by the fact that the His transporter, LAT1, is highly expressed in the BBB endothelium, apart from tumor tissues.[52] Yet, LAT1 is not the ideal target for brain delivery since the transporter easily achieves saturation by plasma amino acids,[53] while LDLR is widely known for its rapidly recycling vesicles and one of the highest BBB trafficking capacity.[54] Interestingly, CL-ANG2-NPs provided a slightly higher BBB permeability compared to H-NPs but, more important, significantly outperformed NCL-ANG2-NPs (Figure 6A). A strong basis for this finding is the study of Clark and Davis who played around ligand-receptor avidity and receptor-mediated BBB trafficking, by designing a tailored BBB endosomal pH acid-sensitive nanosystem.[15] The authors demonstrated that an acid-cleavable transferrin moiety provided considerably higher brain parenchyma levels of NPs upon systemic administration in mice, while the non-cleavable control remained mostly retained in the BBB endothelium. High avidity is thus of uppermost importance to promote receptor binding on the luminal side of the BBB, but should be shifted to mild to low avidity during BBB trafficking to allow proper detachment from the receptor and complete the full transport from blood to brain.[15,55]

The ability of the dual-ligand functionalized NPs to improve BBB permeation was then compared to the simpler system, H-NPs. H-CL-ANG2-NPs increased the permeability levels by approximately two times (Figure 6A). This could result from a cumulative effect of His and the acid-cleavable Angiopep-2 moiety, and suggested that steric hindrance is not interfering with the activity of the nanosystems presenting dual-ligand functionalization. Steric hindrance was possibly avoided by the careful design of two different PEG length levels on the NP surface, namely of 2K (His attachment) and 5K (Angiopep-2 attachment). On the other hand, H-NCL-ANG2 NPs did not present biological advantage over H-NPs regarding BBB permeability (Figure 6A). BBB in vitro model transendothelial electrical resistance (TEER) was monitored over maintenance and throughout the permeability experiment (Figure S15, Supporting Information).

NP formulations were also assessed for their BBB endothelial cell uptake in hCMEC/D3 cells, where acid-cleavable CL-ANG2-NPs and H-CL-ANG2-NPs demonstrated the lowest cell internalization among the other NP samples in both mono-ligand and dual-ligand functionalized groups, respectively (MFI values and percentage of positive cells depicted in Figure 6B and Figure S16, Supporting Information, respectively). This is accordance with literature data and highlighted, once more, that a higher BBB retention does not necessarily correlate with a higher BBB permeability, and contrary trends can be actually found.[15,24,55]

2.7. In Vivo Biodistribution, Therapeutic Efficacy and Toxicity after Intravenous Administration—L-Histidine Plus Acid-Cleavable Angiopep-2 Functionalized Nanoparticles

An in vivo biodistribution screening trial was performed in a healthy mice model, since there is strong and recent evidence that GBM possesses a gross region beyond the contrast-enhancing tumor bulk with an intact BBB, especially at the invasive margins.[56] Thus, it is generally admitted that pharmacological approaches that succeed in transposing the healthy BBB have better chances of improving the treatment response in further GBM disease models.[6,57] In order to reduce the number of animals in light of the 3Rs policy, and considering the previous in vitro findings, it was possible to eliminate the nonfunctionalized NP control from this biodistribution trial—nonfunctionalized NPs were unable to provide an improved GBM cell internalization (Figure 3) and cytotoxicity (Figure 4B,D) compared to H-NPs; moreover, nonfunctionalized NPs were unable to potentiate BBB crossing compared to H-NCL-ANG2-NPs and H-CL-ANG2-NPs (Figure 6A). IVIS imaging to track Cy7.5 labeled NPs was performed at 2, 6, and 24 h postadministration. Brain accumulation of the developed formulations followed the trend H-CL-ANG2-NPs

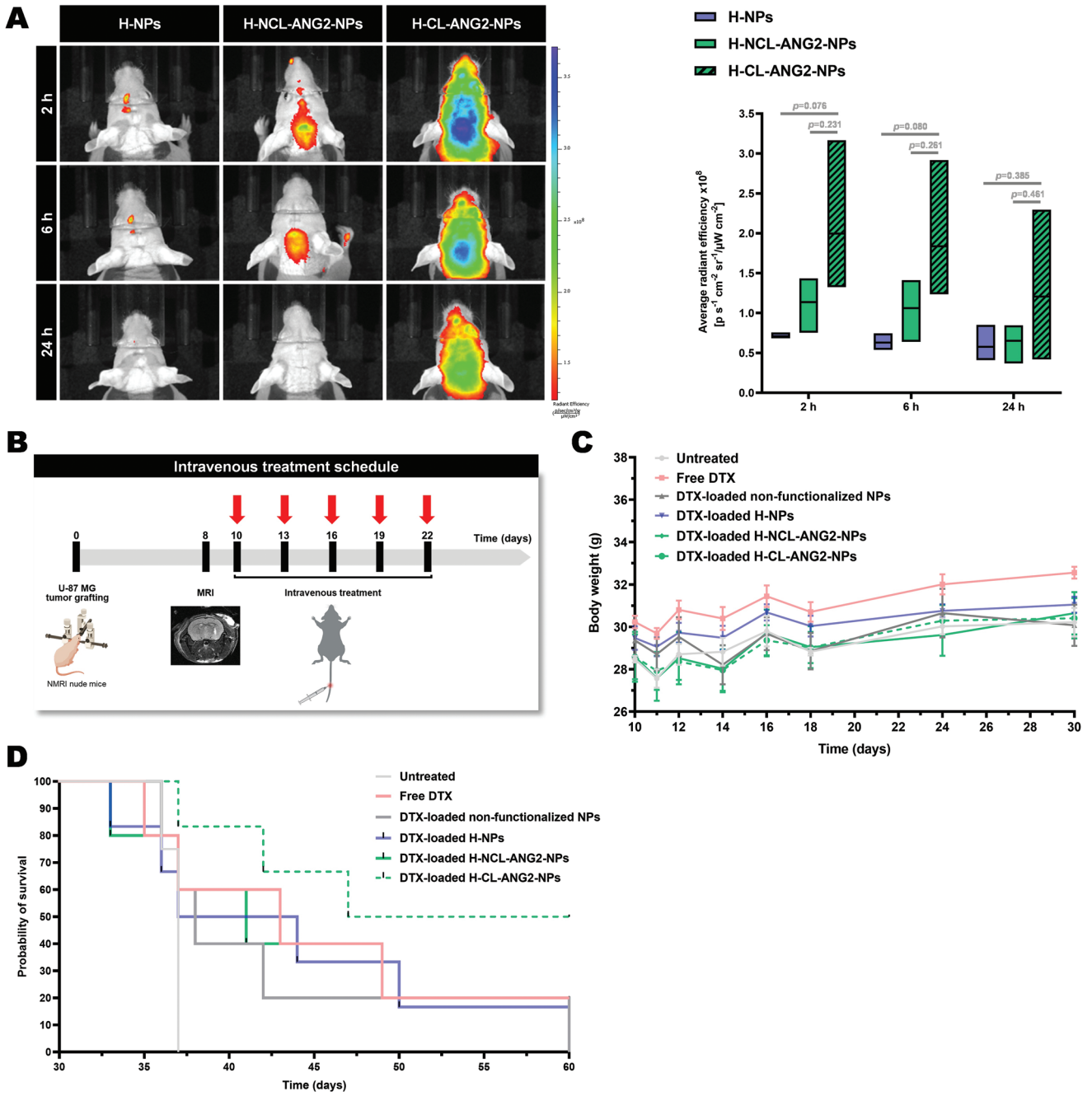

Figure 7. A) In vivo biodistribution of H-CL-ANG2-NPs following intravenous treatment, evidencing brain co-localization of NP formulations at 2, 6, and 24 h postadministration. B–D) In vivo therapeutic efficacy of H-CL-ANG2-NPs following intravenous treatment. NMRI nude mice were orthotopically grafted with U-87 MG GBM cells at day 0, randomized upon MRI tumor evaluation at day 8, and treated with a 2 mg kg^{-1} DTX dose from day 10, every 3 d, for a total of 5 injections. B) Treatment schedule. C) Body weight follow-up until day 30. D) Mice survival curves until day 60.

> H-NCL-ANG2-NPs > H-NPs, with H-CL-ANG2-NPs outperforming the other formulation counterparts (**Figure 7A**). Actually, differences in the maximum average radiant efficiency observed for H-CL-ANG2-NPs achieved approximately four and three times higher values than H-NPs and H-NCL-ANG2-NPs, respectively. The trend of brain accumulation was similar to the predictions of in vitro studies, highlighting the ability of dual-ligand functionalization and acid-responsiveness to enhance NP permeability across the BBB. All formulations presented a reduced brain signal from 2 h to 24 h, which was expected and can be justified by the physiological clearance of NPs over time. Regarding whole-body biodistribution, NPs were tracked for their accumulation in major organs by excision at 24 h (Figure S17, Supporting Information). No relevant accumulation was found in the heart, liver, and spleen accumulation were expected due to the role of these organs in the reticuloendothelial

system,[58] and a certain degree of accumulation was found in kidneys due to renal excretion.[59] Nevertheless, the liver accumulation of free DTX and nontargeted PLGA-based NPs is reported to be 70- and 12.5 times higher compared with the brain,[60] respectively, which is significantly higher than the values obtained for H-NCL-ANG2-NPs (3 times higher). Interestingly, all NP formulations presented a certain level of accumulation in the lungs, but this was clearly more prominent for the formulations presenting an Angiopep-2 moiety. Since LDLR also plays a vital role in the pulmonary tissue, including regulation of antigen uptake, immune responses and fibrogenesis, the expression of the receptor might induce local sequestration of the NPs.[61]

Lastly, the in vivo antitumor effect of H-CL-ANG2-NPs following intravenous treatment was assessed in a GBM orthotopic mice model. Five independent injections starting at day 10 were administered every 3 d at a 2 mg kg^{-1} DTX dose, and survival curves were determined. Body weight was kept stable throughout the treatment course and up to 8 d after the last injection, for all treatment groups (Figure 7C). As presented in Figure 7D and Table 2, the median survival time of the DTX-loaded H-CL-ANG2-NP treatment was 54 days, which presented a significant improvement compared to the untreated (37 d, $*p < 0.05$), free DTX (43 d), DTX-loaded nonfunctionalized NP (38 d), DTX-loaded H-NP (40.5 d) and DTX-loaded H-NCL-ANG2-NP (41 d) groups. Moreover, an increase of more than 50% in the number of survivors at 60 d was observed for DTX-loaded H-CL-ANG2-NPs compared to free DTX, DTX-loaded H-NPs and DTX-loaded H-NCL-ANG2-NPs, whereas there were no 60 d survivors among the untreated and DTX-loaded non-functionalized NP groups. DTX-loaded H-CL-ANG2-NPs outperformed the other NP counterparts, which is in accordance with the higher brain accumulation observed in previous biodistribution studies (Figure 7A) due to the enhanced BBB permeability provided by the acid-cleavable Angiopep-2 moiety of the NPs. Furthermore, once inside the brain parenchyma, adjuvant effect of His is crucial to cause higher DTX accumulation into GBM cells as demonstrated by previous intratumoral therapeutic efficacy in vivo studies (Figure 5D and Table 2). Taken together, more efficient blood-to-brain trafficking and GBM accumulation provided by the acid-cleavable Angiopep-2 and His surface moieties, respectively, endowed H-CL-ANG2-NPs with a potent anti-cancer effect. It is of important note that the DTX dose of each injection, namely 2 mg kg^{-1}, was lower compared to the standard 7.5–10 mg kg^{-1} dose found in literature,[14j,62] but still able to provide a prominent anti-GBM effect. Although our H-CL-ANG2-NP prototype is the first proposed system for both BBB and GBM targeting through the exploitation of a BBB-responsive transport mechanism, we revised literature reports of the past 10 years of multiligand functionalized NPs presenting the same dual-targeting (but lacking BBB responsiveness). By pre-selecting these reports based on the use of the same GBM animal model herein assessed, U-87 MG, the maximum values of median survival were 45 d,[14a] 25 d,[14b] 35 d[14c–f] and 40 d,[14g–i] significantly lower than the median survival obtained for our H-CL-ANG2-NP prototype (54 days). The BBB and GBM dual-targeted system developed by Zhu et al. reached 53 days median survival, but using a DTX dose four times higher than the one herein proposed (2 vs 7.5 mg kg^{-1}).[14j] Specific examples of these literature reported systems include 10 mg kg^{-1} DTX-loaded HRK-19 functionalized poly(lactic acid)-PEG-hyaluronic acid NPs (both hyaluronic acid and HRK-19 for glioma targeting; 40 d median survival; number of long-term survivors not available; C6 GBM bearing rats),[62a] 10 mg kg^{-1} DTX-loaded Angiopep-2 functionalized solid lipid NPs (39 d median survival; no long-term survivors at 60 d; GL261 GBM bearing mice),[63] 7.5 mg kg^{-1} DTX-loaded Angiopep-2 and TAT peptide functionalized micelles (TAT for glioma targeting; 53 d median survival; no long-term survivors at 60 d; U87-MG bearing mice),[14j] 6 mg kg^{-1} DTX-loaded TGN peptide and AS1411 aptamer functionalized PEG-polycaprolactone NPs (TGN and AS1411 for BBB and glioma targeting, respectively; 25 d median survival; no long-term survivors at 60 d; C6 GBM bearing mice),[64] and 5 mg kg^{-1} DTX-loaded RGV29 peptide functionalized PLGA-PEG NPs (RGV29 for both BBB and glioma targeting; 42 d median survival; no long-term survivors at 60 d; C6 GBM bearing rats).[65] This literature review highlights the therapeutic advantage of the H-CL-ANG2-NPs developed under the scope of this work, and the promising potential of this nanotherapy to increase the survival number of GBM patients in the future. Overall, our findings presented strong evidence that both the acid-cleavable properties of the Angiopep-2 moiety and the presence of the His moiety in the stimuli-responsive multifunctional NPs herein proposed are paramount to achieve higher BBB permeation and accumulation at the brain parenchyma GBM cells, respectively, resulting in a better therapeutic effect.

Finally, possible systemic toxicity effects resulting from the intravenous administration of non-nanoparticulate free DTX and NP formulations were assessed, 48 h after treatment. Anticancer therapies often cause severe systemic side effects which directly affect the histological morphology of off-target major organs, organ weight coefficient (organ to body weight normalization), total blood cell count, and blood biochemical parameters. In what concerns histopathological analysis of off-target major organs (heart, liver, lungs, spleen, and kidneys), no morphological signs of damage were found for the free DTX and DTX-loaded NP formulations (**Figure 8**A, Supporting Information), probably due to the low dose of DTX used per administration, namely 2 mg kg^{-1}. Similarly, as shown in Figure S18 (Supporting Information), no significant alterations were found for the brain, heart, liver, lungs, spleen, and kidneys weight coefficients compared with the untreated group. Moreover, none of the drug treatments induced significant differences in the total blood cell count of mice (Figure 8B). Lastly, blood biochemistry parameters, including blood urea nitrogen, creatinine, albumin, aspartate aminotransferase, alanine aminotransferase, total bilirubin, and total protein levels, were assessed to investigate kidney and liver function, as well as possible signs of infection or inflammation. Compared with the untreated animals, mice treated with free DTX or DTX-loaded NPs did not present significant alterations in any of these blood parameters. Altogether, apart from being relatively safe from negligible loss of weight over the treatment course, the stimuli-responsive multifunctional NP therapy herein proposed presented lack of toxicity regarding alterations in histological, hematologic and blood biochemical indicators, as well as organ weight indices.

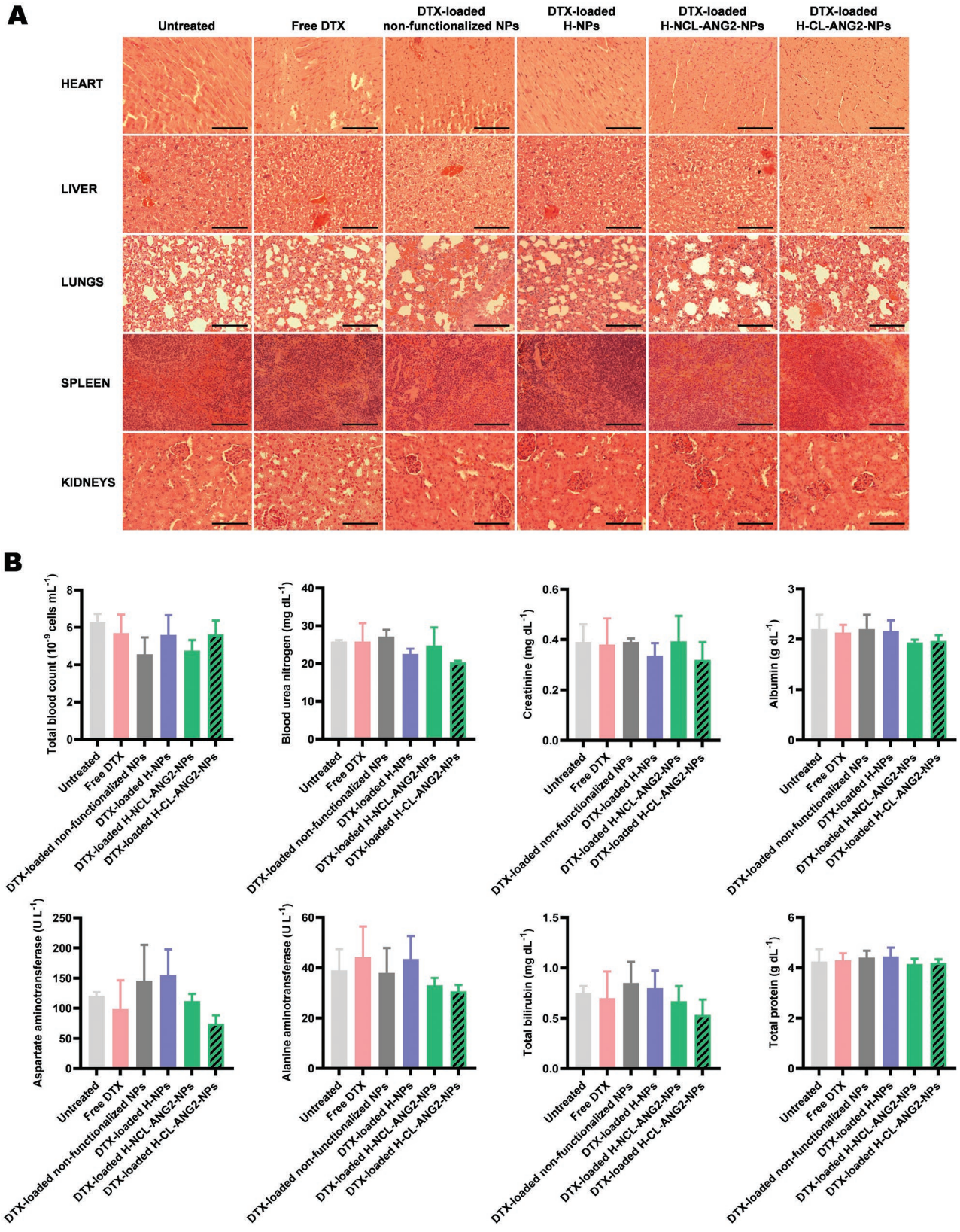

Figure 8. In vivo safety evaluation after intravenous treatment with the developed DTX-loaded NP formulations and free DTX. A) Histopathological analysis of off-target major organs of treated animals by H&E stainings. Scale bars represent 100 µm. B) Evaluation of total cell counts and blood biochemistry parameters of treated animals. NMRI nude mice were orthotopically grafted with U-87 MG GBM cells at day 0, randomized upon MRI tumor evaluation at day 8, and treated with a 2 mg kg^{-1} DTX dose from day 10.

3. Conclusion

In this study, stimuli-responsive multifunctional NPs for the delivery of DTX to GBM were developed envisaging BBB targeting and transport to brain, structural rearrangement within the acidic pH of BBB endosomal vesicles (acid-cleavable Angiopep-2 grafting), and enhancement of GBM cell accumulation post-BBB trafficking (His grafting). These multifunctional NPs increased tumor cell uptake, through the use of the His moiety, by up to four times in GBM conventional cell lines. Due to the relevance of tumor invasive margins in the recurrence and therapeutic resistance of GBM, GIN cells isolated from patient samples were further used. Herein, multifunctional NPs provided up to 12 times higher GBM cell internalization, and up to 3 times higher cytotoxicity in 2D and 3D cell models. After an in vivo intratumoral treatment, NPs presenting the His moiety significantly improved the median survival of mice bearing orthotopically implanted U-87 MG tumors compared to non-functionalized NPs and free DTX. By adding an acid-cleavable Angiopep-2 moiety, with adjuvant effect of the His moiety, the multifunctional NPs presented an increased blood-to-brain transport, by more than threefold, in a BBB in vitro model. In vivo studies in a mice model revealed a clearly higher brain accumulation for these multifunctional NPs, compared to the other NP controls. Lastly, following intravenous treatment at a low DTX dose, the multifunctional NPs increased the median survival of mice by around 20 d and long-term survivors by more than 50%. Moreover, no significant systemic toxicity-related alterations were observed in off-target organs histopathology and weight indices, as well as in blood total cell counts and biochemical indicators. Taken together, the hypothesis proven by our study revealed the key role of both acid-sensitive bioresponsive properties, and BBB and GBM dual-ligand targeting, to achieve an effective multistage anti-GBM therapy. It is of important note to highlight the versatility of the stimuli-responsive multifunctional NPs herein proposed – if in one hand they were proved effective for GBM treatment, they might be also useful in future treatments for brain metastasis and lower grade gliomas; on the other hand, the PLGA core of the NP system has been proved extremely versatile to allow coencapsulation of therapeutic molecules, which might be useful to include alternative chemotherapies or even immunotherapeutics.

4. Experimental Section

Materials: All material sources are detailed in Supporting Information.

Chemical Synthesis of the L-Histidine Functionalized Targeting Polymeric Conjugate: A solution of COOH-L-Histidine-BOC (COOH-His-BOC, MW ≈ 0.255 kDa, 30.6 mg, 120 µmol), N-hydroxysuccinimide (41.4 mg, 360 µmol), and N,N-dicyclohexylcarbodiimide (74.3 mg, 360 µmol) in 9 mL anhydrous dimethylformamide was treated with PLGA-PEG(2K)-NH_2 (Mn ≈ 17 kDa, 360 mg, 22 µmol) and N,N-diisopropylethylamine (37.8 mg, 293 µmol) in 5 mL anhydrous dimethylformamide. The reaction was stirred for 24 h at room temperature (RT) under inert atmosphere. The resultant mixture was poured into cold diethyl ether (80 mL), washed three times with methanol (40 mL) and dried under vacuum overnight. The polymeric conjugate was re-dissolved and filtered in 15 mL anhydrous dichloromethane, and dried under vacuum overnight. The obtained polymeric conjugate, termed PLGA-PEG(2K)-His-BOC, was obtained with 70% yield. A selective carbamate hydrolysis was employed to remove the -BOC protecting group, giving PLGA-PEG(2K)-His (Supporting Information).

Chemical Synthesis of the Cleavable and Noncleavable Angiopep-2 Functionalized Targeting Polymeric Conjugates: Angiopep-2 containing a N-terminal cysteine (MW ≈ 2.405 kDa, 15.45 mg, 6.4 µmol) was treated with tris(2-carboxyethyl)phosphine (3.8 mg, 13.2 µmol) in 8 mL anhydrous dimethylformamide and stirred for 1 h at RT under inert atmosphere. 150 mg of either PLGA-acetal-PEG(5K)-Mal (acid-cleavable, Mn ≈ 35 kDa, 4.3 µmol) or PLGA-PEG(5K)-Mal (non-cleavable, Mn ≈ 35 kDa, 4.3 µmol) dissolved in 2 mL anhydrous dimethylformamide were then added to the mixture, and allowed to react for 24 h at 4 °C under inert atmosphere. The reaction mixture was poured into cold diethyl ether (40 mL), washed three times with methanol (30 mL) and dried under vacuum overnight, giving the cleavable PLGA-acetal-PEG(5K)-ANG2, or the noncleavable PLGA-PEG(5K)-ANG2, with 85% yield.

Characterization of the Targeting Polymeric Conjugates: FTIR spectra were recorded with a FTIR-RAMAN Perkin Elmer 2000 (Perkin Elmer, USA) spectrometer using the potassium bromide (KBr) pellet method. Each pellet was prepared by blending 2 mg of the polymeric conjugate with 200 mg KBr. After a 5 min purge of the sample chamber with N_2, IR spectra were immediately recorded by the accumulation of 200 interferograms at a 4 cm^{-1} spectral resolution over the range from 400 to 8000 cm^{-1} with background subtraction. MALDI-TOF MS was carried out on a Bruker Autoflex III with NdYAG laser (Bruker Corporation, USA), operating in reflector-positive mode. Samples were dissolved in acetonitrile at 2.5 mg mL^{-1} and mixed with the matrix (α-cyano-4-hydroxycinnamic acid, 10 mg mL^{-1} in 50% v/v acetonitrile) in a 1:2 matrix:sample proportion. ^{1}H NMR measurements were performed with a BRUKER AVANCE III 400 MHz (Bruker Corporation, USA) or Bruker Avance III HD 600 MHz (Bruker Corporation, USA) spectrometers at 25°C in deuterated dichloromethane or dimethyl sulfoxide. Chemical shifts are reported in ppm (δ units) and were referenced to the residual solvent signal. Bradford assay was used to quantify the amount of Angiopep-2 in the reaction supernatants. Coomassie Reagent (150 µL) was added to the same volume of each sample in a 96-well plate, and shaken during 30 s. Then, the plate was incubated for 10 min at RT, and the absorbance was measured at 595 nm in a SynergyMx MultiMode microplate reader (BioTek, USA). Angiopep-2 standards were prepared. For testing the acid-cleavable properties of PLGA-acetal-PEG(5K)-Mal, 40 mg of the polymer were suspended in an acetate buffer solution (1 M, pH 5.5), vortexed and left overnight under vigorous stirring. Afterwards, the polymer was recovered by centrifugation, washed three times with water and freeze dried (FreeZone 6, Labconco, USA). The dried polymer was dissolved in dichloromethane (2 mL), the solution poured into cold diethyl ether (10 mL), washed three times with methanol (10 mL) and dried under vacuum overnight. The polymeric conjugate was analyzed by ^{1}H NMR in deuterated dimethylsulfoxide.

Cell Culturing: U-87 MG, U-251-MG, U-373 MG, non-tumor astrocytes (NHA) and GIN cells were cultured in high-glucose Dulbecco's modified Eagle's medium (DMEM), supplemented with fetal bovine serum (FBS, 10% v/v) and penicillin–streptomycin (1% v/v). GIN cells were derived from the infiltrative margin of GBM adult patients undergoing 5-aminolevulinic acid (5ALA, Gliolan) fluorescence guided neurosurgical resection at the Queen's Medical Centre (Nottingham, UK), and obtained from Dr Ruman Rahman. The full protocol for cell isolation[41] and cell authentication details[66] are reported elsewhere. Patient cell origin and single tandem repeat (STR) genotyping data are detailed in Table S1 (Supporting Information). hCMEC/D3 cells were maintained in endothelial basal medium-2 supplemented with FBS (5% v/v), penicillin–streptomycin (1% v/v), hydrocortisone (1.4×10^{-6} M), ascorbic acid (5 µg mL^{-1}), chemically defined lipid concentrate (1/100 v/v), 4-(2-hydroxyethyl)-1-piperazineethanesulphonic acid (10×10^{-3} M) and basic fibroblast growth factor (1 ng mL^{-1}). This last supplement was added extemporaneously in the culture medium. Cell cultures were kept in an incubator (CellCulture CO_2 incubator, ESCO GB Ltd., UK) at 37 °C with 5% CO_2 and 95% relative humidity. Cell culture medium was changed every 2–3 d.

Nanoparticle Manufacture: The microfluidic protocol for NP manufacture was adapted from elsewhere.[20] Briefly, the organic phase consisted of a polymer solution at 40 mg mL^{-1} (TPC based on PLGA-COOH, Mn ≈ 35 kDa, and each targeting polymeric conjugate at the desired percentage) and DTX at 2 mg mL^{-1} in acetonitrile, whereas the aqueous phase consisted of a 1% (w/v) Poloxamer 407 aqueous solution. Both phases were injected into a X-junction microfluidic chip with a three-inlet layout, in which the organic (0.75 mL min^{-1}) and aqueous (2.25 mL min^{-1}) phases were injected through the central and the two outer inlets, respectively. Each experiment was conducted until 20 mg of NPs were produced (equivalent to a 40 s run time). NPs were washed three times with water and recovered by ultrafiltration using Amicon Ultra-15 centrifugal filter units. For the obtention of fluorescent labeled NPs, 10% of the polymer content of the organic phase consisted of either PLGA-FKR648 (Mn ≈ 20 kDa) or PLGA-FITC (Mn ≈ 25 kDa), or DTX in the organic phase was replaced by Cy7.5 carboxylic acid at 0.1 mg mL^{-1} in acetonitrile. To manufacture PEGylated but non-targeted NP controls, mPEG(2K)-PLGA (Mn ≈ 17 kDa) or mPEG(5K)-PLGA (Mn ≈ 35 kDa) were included in the polymer content of the organic phase, giving NP formulations termed mPEG(2K) NPs and mPEG(5K) NPs, respectively.

Flow Cytometry Analysis: 0.25×10^6, 0.3×10^6, or 0.5×10^6 cells per well were seeded for U-87 MG/U-251 MG/U-373 MG (six-well plate) cells, GIN primary cells (six-well plate) and hCMEC/D3 cells (24-well plate),[67] respectively. The cells were allowed to attach overnight, washed with phosphate-buffered saline (PBS), and PLGA-FKR648 or PLGA-FITC labeled NPs in medium (25 µg mL^{-1} or 300 µg mL^{-1}, respectively, 1 mL) were added for 4 h at 37 °C. Afterward, cells were washed twice with PBS, detached with trypsin (50/250 µL), and 150/500 µL media were added to each well. Cells were subsequently washed with PBS, fixed with 2% paraformaldehyde (PFA) for 20 min at RT, washed again, and placed into cytometer tubes for further analysis. Cells were analyzed using an Accuri C6 cytometer (BD Biosciences, USA). MFI was measured for at least 10 000 viable plus single cell gated events per sample, and all data were processed with FlowJo software (Tree Star, USA). Experiments were performed at least in triplicate.

Confocal Microscopy Analysis: GIN cells were seeded in 13 mm diameter glass coverslips placed into 24-well plates (0.06×10^6 cells per coverslip, 400 µL medium), and allowed to attach overnight. The coverslips were precoated with human fibronectin at 2 µg cm^{-2} for 24 h at 37 °C. The cells were washed with PBS, and PLGA-FKR648 labeled NPs in medium (25 µg mL^{-1}, 1 mL) were added and incubated for 4 h at 37 °C. After incubation, the cells were washed twice with PBS, fixed with 2% PFA for 20 min at RT, and washed again. The cells were then permeabilized with 0.25% Triton-X100 (400 µL) for 10 min at RT, and rinsed with PBS. The cells were blocked in 10% FBS in PBS for 30 min at RT. The solution was then replaced by 400 µL of 10% FBS in PBS containing Alexa Fluor 546 labeled-phalloidin (1:200 dilution) and incubated for 20 min at RT. The cells were rinsed three times with PBS, the coverslips were mounted on glass microscope slides with mounting media and dried overnight at RT in the dark. Cells were imaged with a SP5 confocal microscope (Leica Microsystems, Germany) and image analysis was performed with the LAS AF Lite software (Leica). The images are shown as maximum projections of 10–20 Z-stacks with a distance of 1–2 µm between them.

Evaluation of Cell Metabolic Activity (2D): For 2D cultures, 0.002×10^6 GIN cells per well were seeded in 96-well plates and allowed to attach during 48 h, in order to reach a starting confluence level of around 20–30%. After that, the medium was removed, cells were washed three times with PBS, and different concentrations of drug or NP samples (0.00045 to 4.5×10^{-6} M, in regard to the drug) in medium (200 µL) were incubated up to 48 h or 96 h, at 37 °C. For dynamic-like boost treatments, the same procedure was followed, but 4.5×10^{-6} M and 45×10^{-6} M concentrations of drug or NP samples in medium were added for 4 h, cells washed three times with PBS and incubated with fresh medium up to 96 h. At each timepoint, the medium was removed and 200 µL resazurin (20%, v/v) in media was added to each well and incubated for 4 h at 37 °C in the dark. After, fluorescence was measured at the excitation and emission wavelengths of 530 and 590 nm, respectively, using a SynergyMx MultiMode microplate reader (BioTek, USA). Experiments were performed at least in quadruplicate, and all data were normalized in regard to the negative (1% Triton X-100) and positive (medium) controls, which were considered 0% and 100% metabolic activity, respectively. Graphical data for cell metabolic activity was referenced to a threshold of 70% cell viability according to the ISO 10993-5 standard.[68]

Evaluation of Cell Metabolic Activity (3D): GIN spheroids were formed using commercially available micromolds (3D Petri Dish, MicroTissues, USA). Agarose was dissolved at 2% (w/v) in 0.9% NaCl (w/v) and cast into 3D Petri Dish molds to form hydrogel micro-molds with 81 homogenous circular recesses. 0.0025×10^6 cells per spheroid was added to the micromolds and allowed to settle for 30 min, before adding media (2 mL) to each well. Media was replaced every 2 d. Spheroids size was assessed using a ZOE Fluorescent Cell Imager (Bio-Rad Laboratories, USA), and considered the average of two diameter measurements was randomly evaluated in three different spheroids per micromold core. Two days after seeding, medium was removed, micromolds were washed with PBS, and different concentrations of drug or NP samples (0.00045 to 4.5×10^{-6} M, in regard to the drug) in medium (190 µL per micro-molds and 2 mL per well) were added and incubated up to 48 h and 96 h, at 37 °C. For dynamic-like boost treatments, the same procedure was followed, but 4.5×10^{-6} M and 45×10^{-6} M concentrations of drug or NP samples in medium were added for 4 h or 12 h, micromolds washed three times with PBS and incubated with fresh medium up to 96 h. At each time point, the medium was removed and the spheroids were transferred to a 15 mL plastic tube. Per tube, spheroids were incubated with Versene (300 µL) for 10 min and 1× TrypLE Select (200 µL) for 15 min, followed by vigorous pipetting to dissociate the spheroids into single cells. Versene and TrypLE Select were used to promote the weakness of cell–cell adhesion bonds and foster the preservation of surface transporters during dissociation, respectively. The cells were afterward washed three times with PBS and resuspended in 200 µL media, from which 30 µL were transferred to 96-well plates and allowed to attach overnight. The following day, 200 µL resazurin (20%, v/v) in media was added to each well and incubated for 4 h at 37 °C in the dark. After, fluorescence was measured at the excitation and emission wavelengths of 530 and 590 nm, respectively, using a SynergyMx MultiMode microplate reader (BioTek, USA). Experiments were performed at least in quadruplicate, and all data were normalized in regard to the positive control (medium), which was considered 100% metabolic activity. Graphical data for cell metabolic activity was referenced to a threshold of 70% cell viability according to the ISO 10993-5 standard.[68]

Assessment of Blood-Brain Barrier Permeability: The protocol to set up a BBB in vitro model was followed from elsewhere.[69] 0.025×10^6 cells cm^{-2} hCMEC/D3 cells in media (500 µL) were seeded in the apical side on 12-Transwell cell culture inserts. Previously to the seeding, inserts were coated with 90 µL of 50 µg mL^{-1} rat tail collagen type I in acetic acid (0.02 M) for 1 h, at 37 °C, and then washed twice with PBS. The basolateral side was filled with 1.5 mL medium. The model was kept at 37 °C during 8 d, and the medium changed every 2 d. The hCMEC/D3 cell monolayer became confluent at day 8, which was the day selected to initiate the permeability study. The integrity of the cell monolayer was checked every 2 d by monitoring the TEER using an endothelial Volt–Ohm meter (Millicell ER S-2; Merck Millipore, USA). The resistance value of an empty filter was subtracted from each measurement. The permeability experiment was performed in the apical-to-basolateral direction. The apical compartment was filled with FITC-labeled NPs in Hanks' balanced salt solution (300 µg mL^{-1}, 500 µL).[67] Then, the assay was conducted at 37 °C using an orbital shaker incubator (100 rpm). At 24 h, 200 µL samples were taken from the basolateral side and the fluorescence signal was measured at the excitation and emission wavelengths of 490 nm and 520 nm, respectively, using a SynergyMx MultiMode microplate reader (BioTek, USA). Experiments were performed in triplicate.

In Vivo Studies: All experiments were performed following the Belgian national regulations guidelines as well as in accordance with EU Directive 2010/63/EU, and were approved by the ethical committee for animal care of the Université catholique de Louvain (2019/UCL/MD/004). Seven week old female NMRI nude mice (Janvier Labs, France) were given free access to water and food.

In Vivo Biodistribution: To assess Cy7.5 labeled NP biodistribution, mice were intravenously injected with a NP dose equivalent to 10 µg Cy7.5 per animal (110-130 µL injection in PBS, $n = 3$). Biodistribution was visually observed using a Xenogen IVIS 50 imaging system (PerkinElmer, Belgium) at 2, 6, and 24 h after injection. At 24 h, mice were sacrificed, and major organs (heart, lungs, liver, kidneys, spleen) were excised for ex vivo analysis. Regions of interest (ROI) were drawn over the signals and area-normalized average radiant efficiency was quantified in [p s^{-1} cm^{-2} sr^{-1}/µW cm^{-2}]. Results are represented as floating bar plots using minimum and maximum values with a line at the mean.

In Vivo Therapeutic Efficacy: Mice were anesthetized by intraperitoneal injection of ketamine/xylazine (100/13 mg kg^{-1}, respectively) and fixed in a stereotactic frame. A hole was drilled using a surgical high-speed drill (Velleman, Belgium) and 2 µL of DMEM containing 3×10^4 U-87 MG cells were injected into the right hemisphere using an infusion syringe pump (Harvard Apparatus, USA) mounted with a Hamilton syringe (26S gauge needle) as previously described.[70] The injection coordinates were 0.5 mm anterior or posterior, 2.1 mm lateral from the bregma and 2.5–3 mm deep from the outer border of the cranium, respectively. The presence, volume, and location of the tumors were determined by magnetic resonance imaging (MRI, 11.7T Bruker Biospec, Bruker, Germany) at day 8 post U-87 MG cell inoculation. The tumor volume was assessed using the rapid acquisition with relaxation enhancement (RARE) sequence (TR = 2500 ms; effective echo time (TEeff) = 30 ms; RARE factor = 8; FOV = 2 × 2 cm; matrix 256 × 256; 25 contiguous slices of 0.3 mm, NA = 4). At day 10 post U-87 MG cell inoculation, treatments were initiated. For intratumoral treatment, the same coordinates of U-87 MG cell inoculation were used, and 2 µg DTX in 7.5 µL were injected per brain ($n = 8$)– Group 1: untreated; Group 2: free DTX (solubilized in three times diluted Taxotere vehicle); Group 3: nonfunctionalized NPs; Group 4: H-NPs. For intravenous treatment, 2 mg kg^{-1} DTX in 150 µL were injected per animal ($n = 6$), every 3 d, for a total of 5 injections—Group 1: untreated; Group 2: free DTX (solubilized in Taxotere vehicle); Group 3: nonfunctionalized NPs; Group 4: H-NPs; Group 5: H-NCL-ANG2-NPs; Group 6: H-CL-ANG2-NPs.

In Vivo Toxicity: 48 h after the previously detailed intravenous treatment, for GBM bearing mice assigned to each treatment group ($n = 3$), animals were anesthetized by intraperitoneal injection of ketamine/xylazine (100/13 mg kg^{-1}, respectively) and blood was collected through the retro-orbital plexus region in lithium heparin tubes (Microvette 500 LH, Sarstedt, Germany). After a 1:5000 dilution in PBS, blood cell counts were determined by direct microscopic counting in a Bürker cell counting chamber (Fisher Scientific, USA). Blood samples were then centrifuged at 1500 *g* for 10 min to obtain the serum. Blood urea nitrogen, creatinine, albumin, aspartate aminotransferase, alanine aminotransferase, total bilirubin and total protein levels were assessed by Vet Test 8008 (IDEXX, USA). Mice were then sacrificed by cervical dislocation and, for histopathological examination of off-target major organs, organs were fixed in 10% neutral buffered formalin, embedded in paraffin blocks, and frozen at 4 °C before 3–5 µm sections were cut and stained with hematoxylin and eosin (H&E). An Olympus optical microscope (Tokyo, Japan) was used to observe the stained slices.

Statistical Analysis: Results are represented as mean ± standard deviation from a minimum of three independent experiments. Statistical analysis was performed by two-way analysis of variance (ANOVA) followed by a post hoc test (Dunnett's test) to compare experimental groups. For in vivo data, survival curves were compared using a log-rank (Mantel–Cox) test. Differences were considered significant at $*p < 0.05$, $**p < 0.01$, or $***p < 0.001$. Statistical analysis was performed with the software GraphPad Prism 9 (GraphPad Software, USA).

Supporting Information

Supporting Information is available from the Wiley Online Library or from the author.

Acknowledgements

This work was supported by the project Norte-01-0145-FEDER-000051—"Cancer Research on Therapy Resistance: From Basic Mechanisms to Novel Targets," supported by Norte Portugal Regional Operational Programme (NORTE 2020), under the PORTUGAL 2020 Partnership Agreement, through the European Regional Development Fund (FEDER) and FCT - Fundação para a Ciência e a Tecnologia in the framework of the Ph.D. scholarship of CM [SFRH/BD/137946/2018]. This publication is based upon work from COST Action CA 17140 "Cancer Nanomedicine from the Bench to the Bedside" and COST Action CA 17104 " New diagnostic and therapeutic tools against multidrug resistant tumors" supported by COST (European Cooperation in Science and Technology). This work was also supported by European Association for Cancer Research and Worldwide Cancer Research. The authors acknowledge the support of the i3S Scientific Platforms Bioimaging and Histology and Electron Microscopy (HEMS), members of the national infrastructure PPBIPortuguese Platform of Bioimaging (PPBI-POCI-01-0145-FEDER-022122). The authors also acknowledge the support of the Biochemical and Biophysical Technologies, Biointerfaces and Nanotechnology, and Translational Cytometry i3S Scientific Platforms. Centro de Materiais da Universidade do Porto (CEMUP), particularly Mariana Andrade and Sílvia Maia, are also acknowledged for 1H NMR and MALDI-TOF MS analysis, respectively. A.M. was supported by the Marie Skłodowska-Curie Actions for an Individual European Fellowship under the European Union's Horizon 2020 research and innovation program (grant agreement no. 887609) and by Fonds de la Recherche Scientifique–Fonds National de la Recherche Scientifique (FRS-FNRS) (grant agreement no. 40000747) (Belgium). V.P. was supported by FRS-FNRS (grant agreements no. 33669945, 40003419). The authors acknowledge the crucial assistance of Nuno Mendes and Rossana Correia with histology experiments; Emília Cardoso with flow cytometry experiments; Maria Lázaro with confocal microscopy experiments; and Dr Bruno Costa for providing the non-tumor astrocyte cell line.

Conflict of Interest

The authors declare no conflict of interest.

Data Availability Statement

The data that support the findings of this study are available from the corresponding author upon reasonable request.

Keywords

blood-brain barrier, drug delivery, dual-ligand functionalization, glioblastoma, nanomedicine, stimuli-responsiveness, targeting

Received: January 2, 2023
Published online:

[1] H. Sung, J. Ferlay, R. L. Siegel, M. Laversanne, I. Soerjomataram, A. Jemal, F. Bray, *Ca-Cancer J. Clin.* **2021**, *71*, 209.
[2] M. W. Yu, D. F. Quail, *Front. Immunol.* **2021**, *12*, 676301.
[3] W. Yang, J. Soares, P. Greninger, E. J. Edelman, H. Lightfoot, S. Forbes, N. Bindal, D. Beare, J. A. Smith, I. R. Thompson, S. Ramaswamy, P. A. Futreal, D. A. Haber, M. R. Stratton, C. Benes, U. McDermott, M. J. Garnett, *Nucleic Acids Res.* **2012**, *41*, D955.
[4] a) S. Ostermann, C. Csajka, T. Buclin, S. Leyvraz, F. Lejeune, L. A. Decosterd, R. Stupp, *Clin. Cancer Res.* **2004**, *10*, 3728;

b) A. J. ten Tije, W. J. Loos, M. Zhao, S. D. Baker, R. H. Enting, H. van der Meulen, J. Verweij, A. Sparreboom, *Anticancer Drugs* **2004**, *15*, 715.
[5] S. Wilhelm, A. J. Tavares, Q. Dai, S. Ohta, J. Audet, H. F. Dvorak, W. C. W. Chan, *Nat. Rev. Mater.* **2016**, *1*, 16014.
[6] S. Quader, K. Kataoka, H. Cabral, *Adv. Drug Delivery Rev.* **2022**, *182*, 114115.
[7] C. Martins, F. Sousa, F. Araújo, B. Sarmento, *Adv. Healthcare Mater.* **2018**, *7*, 1701035.
[8] M. Souri, M. Soltani, F. Moradi Kashkooli, M. Kiani Shahvandi, M. Chiani, F. S. Shariati, M. R. Mehrabi, L. L. Munn, *Mater. Today Bio* **2022**, *13*, 100208.
[9] A. M. Wagner, D. S. Spencer, N. A. Peppas, *J. Appl. Polym. Sci.* **2018**, *135*, 46154.
[10] X. Zhang, S. Malhotra, M. Molina, R. Haag, *Chem. Soc. Rev.* **2015**, *44*, 1948.
[11] a) W. Zhang, A. Mehta, Z. Tong, L. Esser, N. H. Voelcker, *Adv. Sci.* **2021**, *8*, 2003937; b) A. Duro-Castano, D. Moreira Leite, J. Forth, Y. Deng, D. Matias, C. N. Jesus, G. Battaglia, *Adv. Drug Delivery Rev.* **2020**, *160*, 52.
[12] a) Z. Haining, N. Kawai, K. Miyake, M. Okada, S. Okubo, X. Zhang, Z. Fei, T. Tamiya, *BMC Clin. Pathol.* **2012**, *12*, 4; b) H. Nawashiro, N. Otani, N. Shinomiya, S. Fukui, H. Ooigawa, K. Shima, H. Matsuo, Y. Kanai, H. Endou, *Int. J. Cancer* **2006**, *119*, 484; c) P. Häfliger, R.-P. Charles, *Int. J. Mol. Sci.* **2019**, *20*, 2428.
[13] X. Tian, D. M. Leite, E. Scarpa, S. Nyberg, G. Fullstone, J. Forth, D. Matias, A. Apriceno, A. Poma, A. Duro-Castano, M. Vuyyuru, L. Harker-Kirschneck, A. Šarić, Z. Zhang, P. Xiang, B. Fang, Y. Tian, L. Luo, L. Rizzello, G. Battaglia, *Sci. Adv.* **2020**, *6*, eabc4397.
[14] a) Z. Jin, L. Piao, G. Sun, C. Lv, Y. Jing, R. Jin, *J. Drug Targeting* **2021**, *29*, 323; b) X. Wang, Y. Zhao, S. Dong, R. J. Lee, D. Yang, H. Zhang, L. Teng, *Molecules* **2019**, *24*, 3540; c) S. Lakkadwala, B. dos Santos Rodrigues, C. Sun, J. Singh, *J. Controlled Release* **2019**, *307*, 247; d) C. Liu, Z. Zhao, H. Gao, I. Rostami, Q. You, X. Jia, C. Wang, L. Zhu, Y. Yang, *Nanotheranostics* **2019**, *3*, 311; e) Z. Belhadj, C. Zhan, M. Ying, X. Wei, C. Xie, Z. Yan, W. Lu, *OncoTargets Ther.* **2017**, *8*, 66889; f) J.-Q. Gao, Q. Lv, L.-M. Li, X.-J. Tang, F.-Z. Li, Y.-L. Hu, M. Han, *Biomaterials* **2013**, *34*, 5628; g) X. Zhu, H. Zhou, Y. Liu, Y. Wen, C. Wei, Q. Yu, J. Liu, *Acta Biomater.* **2018**, *82*, 143; h) C. Chen, Z. Duan, Y. Yuan, R. Li, L. Pang, J. Liang, X. Xu, J. Wang, *ACS Appl. Mater. Interfaces* **2017**, *9*, 5864; i) P. Zhang, L. Hu, Q. Yin, L. Feng, Y. Li, *Mol. Pharm.* **2012**, *9*, 1590; j) Y. Zhu, Y. Jiang, F. Meng, C. Deng, R. Cheng, J. Zhang, J. Feijen, Z. Zhong, *J. Controlled Release* **2018**, *278*, 1.
[15] A. J. Clark, M. E. Davis, *Proc. Natl. Acad. Sci. USA* **2015**, *112*, 12486.
[16] C. Cannavà, R. Stancanelli, M. R. Marabeti, V. Venuti, C. Cascio, P. Guarneri, C. Bongiorno, G. Sortino, D. Majolino, A. Mazzaglia, S. Tommasini, C. A. Ventura, *RSC Adv.* **2016**, *6*, 16720.
[17] R. Cheng, A. C. Weitz, J. Paris, Y. Tang, J. Zhang, H. Song, N. Naowarojna, K. Li, L. Qiao, J. Lopez, M. W. Grinstaff, L. Zhang, Y. Guo, S. Elliott, P. Liu, *Chem. Sci.* **2022**, *13*, 3589.
[18] a) F. C. Thomas, K. Taskar, V. Rudraraju, S. Goda, H. R. Thorsheim, J. A. Gaasch, R. K. Mittapalli, D. Palmieri, P. S. Steeg, P. R. Lockman, Q. R. Smith, *Pharm. Res.* **2009**, *26*, 2486; b) F. Marcucci, A. Corti, A. J. M. Ferreri, *Cancers* **2021**, *13*, 2391.
[19] a) L. Costantino, F. Gandolfi, G. Tosi, F. Rivasi, M. A. Vandelli, F. Forni, *J. Controlled Release* **2005**, *108*, 84; b) G. P. Hoyos-Ceballos, B. Ruozi, I. Ottonelli, F. Da Ros, M. A. Vandelli, F. Forni, E. Daini, A. Vilella, M. Zoli, G. Tosi, J. T. Duskey, B. L. López-Osorio, *Pharmaceutics* **2020**, *12*, 72.
[20] a) C. Martins, F. Araújo, M. J. Gomes, C. Fernandes, R. Nunes, W. Li, H. A. Santos, F. Borges, B. Sarmento, *Eur. J. Pharm. Biopharm.* **2018**, *138*, 111; b) C. Martins, V. M. Chauhan, A. A. Selo, M. Al-Natour, J. W. Aylott, B. Sarmento, *React. Chem. Eng.* **2020**, *5*, 308; c) C. Martins, B. Sarmento, in *Drug Delivery Systems* (Ed: K. K. Jain), Springer, New York, NY **2020**, p. 213.
[21] a) R. Juliano, *Nat. Rev. Drug Discovery* **2013**, *12*, 171; b) J. Ma, S. M.-Y. Lee, C. Yi, C.-W. Li, *Lab Chip* **2017**, *17*, 209.
[22] A. Gdowski, K. Johnson, S. Shah, I. Gryczynski, J. Vishwanatha, A. Ranjan, *J. Nanobiotechnol.* **2018**, *16*, 12.
[23] D. Furtado, M. Björnmalm, S. Ayton, A. I. Bush, K. Kempe, F. Caruso, *Adv. Mater.* **2018**, *30*, 1801362.
[24] T. D. Brown, N. Habibi, D. Wu, J. Lahann, S. Mitragotri, *ACS Biomater. Sci. Eng.* **2020**, *6*, 4916.
[25] a) J. Key, A. L. Palange, F. Gentile, S. Aryal, C. Stigliano, D. Di Mascolo, E. De Rosa, M. Cho, Y. Lee, J. Singh, P. Decuzzi, *ACS Nano* **2015**, *9*, 11628; b) Z. Wang, J. Ding, X. Ma, S. Luo, *RSC Adv.* **2018**, *8*, 17958; c) L. Ribovski, E. de Jong, O. Mergel, G. Zu, D. Keskin, P. van Rijn, I. S. Zuhorn, *Nanomedicine* **2021**, *34*, 102377.
[26] T. Tsuji, H. Yoshitomi, J. Usukura, *Microscopy* **2013**, *62*, 341.
[27] P. P. Di Mauro, S. Borrós, *Pharm. Res.* **2014**, *31*, 3461.
[28] a) J. Cheng, B. A. Teply, I. Sherifi, J. Sung, G. Luther, F. X. Gu, E. Levy-Nissenbaum, A. F. Radovic-Moreno, R. Langer, O. C. Farokhzad, *Biomaterials* **2007**, *28*, 869; b) S. Maiolino, A. Russo, V. Pagliara, C. Conte, F. Ungaro, G. Russo, F. Quaglia, *J. Nanobiotechnol.* **2015**, *13*, 29; c) P. Rafiei, A. Haddadi, *Int. J. Nanomed.* **2017**, *12*, 935.
[29] Z. Xiao, E. Levy-Nissenbaum, F. Alexis, A. Lupták, B. A. Teply, J. M. Chan, J. Shi, E. Digga, J. Cheng, R. Langer, O. C. Farokhzad, *ACS Nano* **2012**, *6*, 696.
[30] K. Kobayashi, A. Ohnishi, J. Promsuk, S. Shimizu, Y. Kanai, Y. Shiokawa, M. Nagane, *Neurosurgery* **2008**, *62*, 493.
[31] a) O. Yanagida, Y. Kanai, A. Chairoungdua, D. K. Kim, H. Segawa, T. Nii, S. H. Cha, H. Matsuo, J. Fukushima, Y. Fukasawa, Y. Tani, Y. Taketani, H. Uchino, J. Y. Kim, J. Inatomi, I. Okayasu, K. Miyamoto, E. Takeda, T. Goya, H. Endou, *Biochim. Biophys. Acta* **2001**, *1514*, 291; b) H.-C. Chien, C. Colas, K. Finke, S. Springer, L. Stoner, A. A. Zur, B. Venteicher, J. Campbell, C. Hall, A. Flint, E. Augustyn, C. Hernandez, N. Heeren, L. Hansen, A. Anthony, J. Bauer, D. Fotiadis, A. Schlessinger, K. M. Giacomini, A. A. Thomas, *J. Med. Chem.* **2018**, *61*, 7358.
[32] a) D. Brevet, O. Hocine, A. Delalande, L. Raehm, C. Charnay, P. Midoux, J. O. Durand, C. Pichon, *Int. J. Pharm.* **2014**, *471*, 197; b) V. Jahed, E. Vasheghani-Farahani, F. Bagheri, A. Zarrabi, T. Fink, K. L. Larsen, *Int. J. Nanomed.* **2019**, *14*, 8221; c) G. Tan, J. Li, D. Liu, H. Pan, R. Zhu, Y. Yang, W. Pan, *Int. J. Pharm.* **2021**, *602*, 120641; d) E. Gallon, T. Matini, L. Sasso, G. Mantovani, A. Armiñan de Benito, J. Sanchis, P. Caliceti, C. Alexander, M. J. Vicent, S. Salmaso, *Biomacromolecules* **2015**, *16*, 1924.
[33] S.-Y. Wu, H.-Y. Chou, H.-C. Tsai, R. Anbazhagan, C.-H. Yuh, J. M. Yang, Y.-H. Chang, *RSC Adv.* **2020**, *10*, 20682.
[34] a) L. Li, X. Di, M. Wu, Z. Sun, L. Zhong, Y. Wang, Q. Fu, Q. Kan, J. Sun, Z. He, *Nanomedicine* **2017**, *13*, 987; b) L. Li, X. Di, S. Zhang, Q. Kan, H. Liu, T. Lu, Y. Wang, Q. Fu, J. Sun, Z. He, *Colloids Surf., B* **2016**, *141*, 260.
[35] Z. Wang, D. Chi, X. Wu, Y. Wang, X. Lin, Z. Xu, H. Liu, J. Sun, Z. He, Y. Wang, *J. Controlled Release* **2019**, *316*, 22.
[36] S. Nozaki, Y. Nakatani, A. Mawatari, N. Shibata, W. E. Hume, E. Hayashinaka, Y. Wada, H. Doi, Y. Watanabe, *Sci. Rep.* **2019**, *9*, 15718.
[37] S. Okubo, H.-N. Zhen, N. Kawai, Y. Nishiyama, R. Haba, T. Tamiya, *J. Neurooncol.* **2010**, *99*, 217.
[38] A. Habermeier, J. Graf, B. F. Sandhöfer, J. P. Boissel, F. Roesch, E. I. Closs, *Amino Acids* **2015**, *47*, 335.
[39] A. Hahn, J. Bode, T. Krüwel, G. Solecki, S. Heiland, M. Bendszus, B. Tews, F. Winkler, M. O. Breckwoldt, F. T. Kurz, *Sci. Rep.* **2019**, *9*, 11757.
[40] a) S. L. Perrin, M. S. Samuel, B. Koszyca, M. P. Brown, L. M. Ebert, M. Oksdath, G. A. Gomez, *Biochem. Soc. Trans.* **2019**, *47*, 625;

b) C. E. Vasey, R. J. Cavanagh, V. Taresco, C. Moloney, S. Smith, R. Rahman, C. Alexander, *Pharmaceutics* **2021**, *13*, 208.

[41] a) S. J. Smith, J. Rowlinson, M. Estevez-Cebrero, D. Onion, A. Ritchie, P. Clarke, K. Wood, M. Diksin, A. Lourdusamy, R. G. Grundy, R. Rahman, *Neurooncol. Adv.* **2020**, *2*, vdaa087; b) S. J. Smith, M. Diksin, S. Chhaya, S. Sairam, M. A. Estevez-Cebrero, R. Rahman, *Int. J. Mol. Sci.* **2017**, *18*, 2452.

[42] a) H. Nawashiro, N. Otani, Y. Uozumi, H. Ooigawa, T. Toyooka, T. Suzuki, H. Katoh, N. Tsuzuki, A. Ohnuki, K. Shima, N. Shinomiya, H. Matsuo, Y. Kanai, *Brain Tumor Pathol.* **2005**, *22*, 89; b) D. Y. Lewis, R. Mair, A. Wright, K. Allinson, S. K. Lyons, T. Booth, J. Jones, R. Bielik, D. Soloviev, K. M. Brindle, *Theranostics* **2018**, *8*, 3991.

[43] K. Petrecca, M.-C. Guiot, V. Panet-Raymond, L. Souhami, *J. Neuro-Oncol.* **2013**, *111*, 19.

[44] M. A. Islam, Y. Xu, W. Tao, J. M. Ubellacker, M. Lim, D. Aum, G. Y. Lee, K. Zhou, H. Zope, M. Yu, W. Cao, J. T. Oswald, M. Dinarvand, M. Mahmoudi, R. Langer, P. W. Kantoff, O. C. Farokhzad, B. R. Zetter, J. Shi, *Nat. Biomed. Eng.* **2018**, *2*, 850.

[45] B. Ouyang, W. Poon, Y.-N. Zhang, Z. P. Lin, B. R. Kingston, A. J. Tavares, Y. Zhang, J. Chen, M. S. Valic, A. M. Syed, P. MacMillan, J. Couture-Senécal, G. Zheng, W. C. W. Chan, *Nat. Mater.* **2020**, *19*, 1362.

[46] A. S. Nunes, A. S. Barros, E. C. Costa, A. F. Moreira, I. J. Correia, *Biotechnol. Bioeng.* **2019**, *116*, 206.

[47] T. Bauleth-Ramos, T. Feijão, A. Gonçalves, M.-A. Shahbazi, Z. Liu, C. Barrias, M. J. Oliveira, P. Granja, H. A. Santos, B. Sarmento, *J. Controlled Release* **2020**, *323*, 398.

[48] C. Dubois, R. Dufour, P. Daumar, C. Aubel, C. Szczepaniak, C. Blavignac, E. Mounetou, F. Penault-Llorca, M. Bamdad, *Onco-Targets Ther.* **2017**, *8*, 95316.

[49] a) M. A. G. Barbosa, C. P. R. Xavier, R. F. Pereira, V. Petrikaitė, M. H. Vasconcelos, *Cancers* **2021**, *14*, 190; b) M. E. Ackerman, D. Pawlowski, K. D. Wittrup, *Mol. Cancer Ther.* **2008**, *7*, 2233.

[50] S. J. Yu, J. H. Yoon, J. M. Lee, J. Y. Lee, S. H. Kim, Y. Y. Cho, J. J. Yoo, M. Lee, D. H. Lee, Y. Cho, E. J. Cho, J. H. Lee, Y. J. Kim, C. Y. Kim, *Medicine* **2016**, *95*, e4551.

[51] a) Y. Hao, B. Zhang, C. Zheng, R. Ji, X. Ren, F. Guo, S. Sun, J. Shi, H. Zhang, Z. Zhang, L. Wang, Y. Zhang, *J. Controlled Release* **2015**, *220*, 545; b) H. Xin, X. Sha, X. Jiang, L. Chen, K. Law, J. Gu, Y. Chen, X. Wang, X. Fang, *Biomaterials* **2012**, *33*, 1673; c) M. Liu, A. Apriceno, M. Sipin, E. Scarpa, L. Rodriguez-Arco, A. Poma, G. Marchello, G. Battaglia, S. Angioletti-Uberti, *Nat. Commun.* **2020**, *11*, 4836; d) Y. Jiang, W. Yang, J. Zhang, F. Meng, Z. Zhong, *Adv. Mater.* **2018**, *30*, 1800316.

[52] R. J. Boado, J. Y. Li, M. Nagaya, C. Zhang, W. M. Pardridge, *Proc. Natl. Acad. Sci. USA* **1999**, *96*, 12079.

[53] E. M. del Amo, A. Urtti, M. Yliperttula, *Eur. J. Pharm. Sci.* **2008**, *35*, 161.

[54] Y. Bertrand, J. C. Currie, J. Poirier, M. Demeule, A. Abulrob, D. Fatehi, D. Stanimirovic, H. Sartelet, J. P. Castaigne, R. Béliveau, *Br. J. Cancer* **2011**, *105*, 1697.

[55] D. T. Wiley, P. Webster, A. Gale, M. E. Davis, *Proc. Natl. Acad. Sci. USA* **2013**, *110*, 8662.

[56] a) J. N. Sarkaria, L. S. Hu, I. F. Parney, D. H. Pafundi, D. H. Brinkmann, N. N. Laack, C. Giannini, T. C. Burns, S. H. Kizilbash, J. K. Laramy, K. R. Swanson, T. J. Kaufmann, P. D. Brown, N. Y. R. Agar, E. Galanis, J. C. Buckner, W. F. Elmquist, *Neuro-Oncology* **2017**, *20*, 184; b) A. T. Kessler, A. A. Bhatt, *Insights Imaging* **2018**, *9*, 1057.

[57] M. Osswald, J. Blaes, Y. Liao, G. Solecki, M. Gömmel, A. S. Berghoff, L. Salphati, J. J. Wallin, H. S. Phillips, W. Wick, F. Winkler, *Clin. Cancer Res.* **2016**, *22*, 6078.

[58] K. M. Tsoi, S. A. MacParland, X.-Z. Ma, V. N. Spetzler, J. Echeverri, B. Ouyang, S. M. Fadel, E. A. Sykes, N. Goldaracena, J. M. Kaths, J. B. Conneely, B. A. Alman, M. Selzner, M. A. Ostrowski, O. A. Adeyi, A. Zilman, I. D. McGilvray, W. C. W. Chan, *Nat. Mater.* **2016**, *15*, 1212.

[59] C. Ghimire, H. Wang, H. Li, M. Vieweger, C. Xu, P. Guo, *ACS Nano* **2020**, *14*, 13180.

[60] a) A. K. Mohammad, J. J. Reineke, *Mol. Pharm.* **2013**, *10*, 2183; b) A. A. van der Veldt, N. H. Hendrikse, E. F. Smit, M. P. Mooijer, A. Y. Rijnders, W. R. Gerritsen, J. J. van der Hoeven, A. D. Windhorst, A. A. Lammertsma, M. Lubberink, *Eur. J. Nucl. Med. Mol. Imaging* **2010**, *37*, 1950.

[61] X. Yao, S. J. Levine, *Am. J. Respir. Cell Mol. Biol.* **2021**, *64*, 279.

[62] a) R. Fan, D. Chuan, H. Hou, H. Chen, B. Han, X. Zhang, L. Zhou, A. Tong, J. Xu, G. Guo, *Nanoscale* **2019**, *11*, 11285; b) H. Gao, Z. Yang, S. Zhang, S. Cao, Z. Pang, X. Yang, X. Jiang, *J. Controlled Release* **2013**, *172*, 921.

[63] A. Kadari, D. Pooja, R. H. Gora, S. Gudem, V. R. M. Kolapalli, H. Kulhari, R. Sistla, *Eur. J. Pharm. Biopharm.* **2018**, *132*, 168.

[64] H. Gao, J. Qian, S. Cao, Z. Yang, Z. Pang, S. Pan, L. Fan, Z. Xi, X. Jiang, Q. Zhang, *Biomaterials* **2012**, *33*, 5115.

[65] H. Hua, X. Zhang, H. Mu, Q. Meng, Y. Jiang, Y. Wang, X. Lu, A. Wang, S. Liu, Y. Zhang, Z. Wan, K. Sun, *Int. J. Pharm.* **2018**, *543*, 179.

[66] S. J. Smith, B. M. Tyler, T. Gould, G. J. Veal, N. Gorelick, J. Rowlinson, R. Serra, A. Ritchie, P. Berry, A. Otto, J. Choi, N. Skuli, M. Estevez-Cebrero, K. M. Shakesheff, H. Brem, R. G. Grundy, R. Rahman, *Clin. Cancer Res.* **2019**, *25*, 5094.

[67] M. J. Gomes, C. Fernandes, S. Martins, F. Borges, B. Sarmento, *J. Neuroimmune Pharmacol.* **2016**, *12*, 107.

[68] A. ISO 10993-5: 2009 Biological Evaluation of Medical Devices-Part 5: Tests for in Vitro Cytotoxicity; ISO: Phoenix, USA 2009, *2007*, 1, https://www.iso.org/standard/36406.html (accessed: January 2023).

[69] a) B. Mendes, C. Marques, I. Carvalho, P. Costa, S. Martins, D. Ferreira, B. Sarmento, *Int. J. Pharm.* **2015**, *490*, 94; b) M. J. Gomes, P. J. Kennedy, S. Martins, B. Sarmento, *Nanomedicine* **2017**, *12*, 1385.

[70] a) F. Danhier, K. Messaoudi, L. Lemaire, J. P. Benoit, F. Lagarce, *Int. J. Pharm.* **2015**, *481*, 154; b) J. Bianco, C. Bastiancich, N. Joudiou, B. Gallez, A. des Rieux, F. Danhier, *J. Neurosci. Methods* **2017**, *284*, 96.